NUWC-NPT Technical Report 10,902
3 April 1998

A Method for Passive Imaging of the Left Anterior Descending Coronary Artery in the Presence of Coherent Heart Wall Motion

Andrew J. Hull
Norman L. Owsley
Submarine Sonar Department

Naval Undersea Warfare Center Division
Newport, Rhode Island

PREFACE

This work was performed under the NUWC Division Newport Bid and Proposal Program, Job Order No. 798B058, "Noninvasive Passive Detection, Localization, and Characterization of Early Stage Arterial Disease," principal investigators Andrew J. Hull (Code 2141) and Norman L. Owsley (Code 2123).

The technical reviewer for this report was Ronald R. Kneipfer (Code 215).

The authors wish to thank James B. Donald (Code 019) for his encouragement and support of the project and Karen Holt (Code 5431) for her assistance with the technical editing.

Reviewed and Approved: 3 April 1998

Ronald J. Martin
Head, Submarine Sonar Department

REPORT DOCUMENTATION PAGE

Form Approved
OMB No. 0704-0188

1. AGENCY USE ONLY *(Leave blank)*	2. REPORT DATE	3. REPORT TYPE AND DATES COVERED
	3 April 1998	Final

4. TITLE AND SUBTITLE

A Method for Passive Imaging of the Left Anterior Descending Coronary Artery in the Presence of Coherent Heart Wall Motion

5. FUNDING NUMBERS

6. AUTHOR(S)

Andrew J. Hull
Norman L. Owsley

7. PERFORMING ORGANIZATION NAME(S) AND ADDRESS(ES)

Naval Undersea Warfare Center Division
1176 Howell Street
Newport, RI 02841-1708

8. PERFORMING ORGANIZATION REPORT NUMBER

TR 10,902

9. SPONSORING/MONITORING AGENCY NAME(S) AND ADDRESS(ES)

10. SPONSORING/MONITORING AGENCY REPORT NUMBER

11. SUPPLEMENTARY NOTES

12a. DISTRIBUTION/AVAILABILITY STATEMENT

Approved for public release; distribution is unlimited.

12b. DISTRIBUTION CODE

13. ABSTRACT *(Maximum 200 words)*

This report describes a method to passively image the left anterior descending coronary artery when high-level coherent heart wall energy is present in the immediate vicinity of the artery. It is shown through simulation that a reduced variance distortionless response (RVDR) focused beamformer has the capability to suppress the front heart wall motion caused by blood-flow-induced energy, and can thus properly image the low-signal-level, flow-induced energy from the coronary arteries and the interventricular septum. It is also shown that separating the coronary artery from the septum is a signal-to-noise issue. Human data that are similar to the simulations for imaging the septum region are presented. In addition, other possible energy sources in the data and energy propagation paths are discussed.

14. SUBJECT TERMS

Arterial Disease
Heart Disease
Noninvasive Detection
Beamformed Imaging
Coronary Arteries

15. NUMBER OF PAGES
64

16. PRICE CODE

17. SECURITY CLASSIFICATION OF REPORT	18. SECURITY CLASSIFICATION OF THIS PAGE	19. SECURITY CLASSIFICATION OF ABSTRACT	20. LIMITATION OF ABSTRACT
Unclassified	Unclassified	Unclassified	SAR

TABLE OF CONTENTS

LIST OF ILLUSTRATIONS

LIST OF ILLUSTRATIONS (Cont'd)

LIST OF ILLUSTRATIONS (Cont'd)

LIST OF TABLES

A METHOD FOR PASSIVE IMAGING OF THE LEFT ANTERIOR DESCENDING CORONARY ARTERY IN THE PRESENCE OF COHERENT HEART WALL MOTION

1. INTRODUCTION

Coronary artery disease (CAD) is a primary precursor of heart attacks, the leading cause of death in the United States. CAD is the buildup of plaque in the coronary arteries resulting in a condition referred to as stenosis in which blood flow may be restricted and the oxygen supply to the heart muscle decreased accordingly. Presymptomatic detection of coronary artery stenosis before permanent heart muscle damage has occurred is critical because the disease could be treated with diet and medication rather than with coronary bypass surgery or angioplasty. Early CAD diagnosis on a wide scale would save the U.S. health care system billions of dollars and would preserve the quality of life for those who might otherwise suffer from the debilitating effects of untreated heart disease.

The standard method for locating stenosis in coronary arteries is with an invasive test called an angiogram. During this procedure, a catheter injects a radiopaque fluoroscopic contrast agent into the coronary arteries, allowing the location of arterial blockages to be viewed on a concurrent x-ray. However, an angiogram is costly and places the patient at significant risk.

For many years, nonintrusive ultrasound has been used by cardiologists to image coronary valve action. This technique, which exploits the compressional wave field in the human body, uses a transducer array to transmit low-level energy into the body where it is absorbed and reflected to varying degrees. After the same array receives the energy back, an image is formed with a volume-scanning focused beamformer. Although ultrasound can effectively image the inside of a near-surface artery, such as the carotid artery, it cannot image a coronary artery due to its location deep in a nonhomogeneous medium, its smaller diameter, and the nearby scattering of energy.

The left anterior descending (LAD) artery is the most important coronary artery in a human. From the left coronary ostia, the left main (LM) coronary artery protrudes and bifurcates into the LAD and the left circumflex artery; in some individuals, the LM coronary

artery trifurcates and the middle branch is called the median ramus. The LM, LAD, and the left circumflex arteries all lie very close to or on the heart wall.

The LAD artery runs from the region around the left atrium down the area between the left and right ventricles on the surface of the heart in a slot called the interventricular groove. This artery is divided into four contiguous segments, with six main branches (three of which are septal perforators that separate toward the sternum and enter the heart muscle and three of which are diagonal branches that separate away from the sternum). Directly behind the LAD is the front heart wall and the interventricular septum, which is a wall that separates the left and right ventricles of the heart and is approximately orthogonal to the front heart wall.

To passively image the LAD artery, blood flow in the artery needs to be at or near a maximum. This occurs during the diastolic phase of the heart cycle, when the semilunar valves of the pulmonary artery and the aorta are closed and the tricuspid valve and the bicuspid (mitral) valve are open, with blood flowing from the left and right atriums down into the left and right ventricles, respectively. In diastole, flow through these valves transports energy both along the inner valve surface and to a blood flow jet, which extends into the ventricle below each valve. This jet is characterized by blood mass deceleration and circulating fluid eddies, as illustrated for the left ventricle in figure 1. Energy can be transferred from this area in the form of both compressional waves (emanating from the mitral valve jet) and shear waves (resulting from excitation along the valve's inner surface). The resulting heart wall motion produces spatially coherent energy radiation, which tends to be much stronger than the energy from turbulence in the blood flowing through a partially blocked coronary artery. Because such spatially coherent energy radiation does not produce well-resolved images when processed with conventional time delay-and-sum beamformer processing techniques, the problem of imaging the LAD artery becomes very difficult. Additionally, the LAD artery and the septum (also characterized by the blood-flow-induced motion of the heart wall) are in close proximity and will thus image as one energy source, resulting in further resolution difficulties.

This report presents a method for imaging the LAD artery and the interventricular septum through analysis of sampled time domain measurements of displacements made on the skin in the intercostal region of the human thorax. After these data are edited so that the systolic phase of the heartbeat cycle (including the S1 and S2 sounds) are removed, retaining only diastolic phase time-sampled data, they are transformed into the frequency domain with fast Fourier transformations. The resulting measurements, which contain energy that is predominantly transferred by the shear wave in the surrounding soft tissue, are assembled into multiple-sensor cross-spectral density matrices (CSDM) at each discrete frequency in the

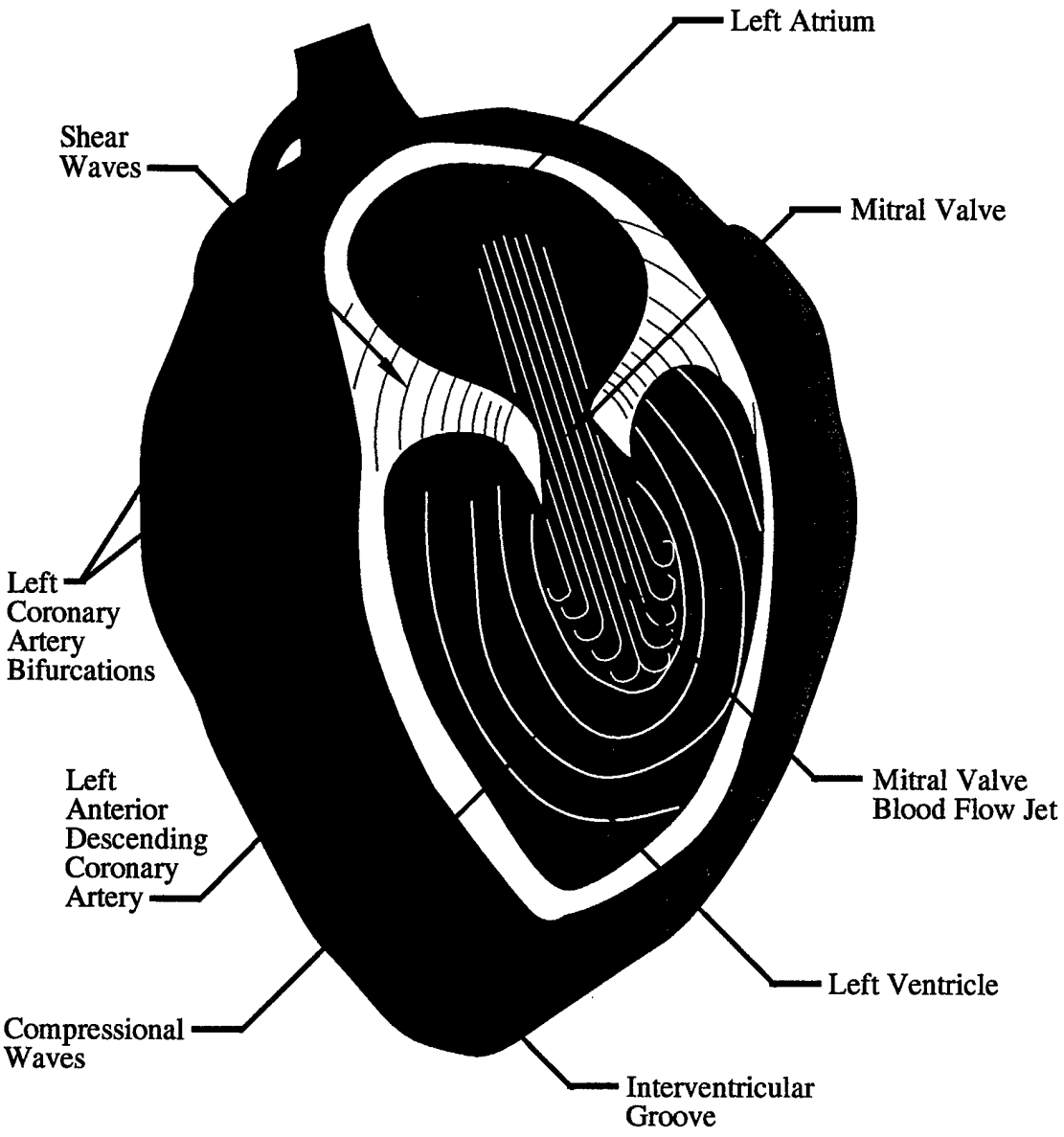

Figure 1. Simplified Diagram of Diastolic Blood Flow Through the Mitral Valve Into the Left Ventricle

analysis band. Beamforming signal processing algorithms are then applied to the CSDM to produce images of the underlying area. It is shown through simulation that a reduced variance distortionless response (RVDR) focused beamformer has the capability to suppress the front heart wall motion caused by blood-flow-induced energy and can thus properly image the low-signal-level, flow-induced energy from the coronary arteries and the interventricular septum. It is also shown that a conventional focused beamformer (CFB) produces valvular energy-masked images of the coronary arteries when coherent heart wall motion is present.

2. IMAGE FORMATION USING FOCUSED BEAMFORMING

Medical imaging involves the mapping of a spatial energy distribution inside the human body. The experimental images produced in this report were generated from data collected with an array of passive sensing devices.[1] These data are assembled into the CSDM and then manipulated with a space-time filter, referred to as a beamformer.[2]

The images produced with the beamformers described below are two-dimensional color plots. The x-axis of each plot is the distance across the medium, and the y-axis is image depth into the medium. The color of the plot indicates the intensity of the energy at a specific location. The image can be visualized as the intensity of distributed energy at the point where a "slice" into the human body is made. The contributions of propagating energy from the heart wall, the septum, and the coronary arteries in the images are discussed in sections 3, 4, and 5.

The beamformer is defined by assuming that $\mathbf{x}(\omega_0)$ is a zero-mean, stationary, complex data vector of N sensor outputs that have been Fourier transformed at fixed frequency ω_0. The image scalar pixel value of the range/depth beamformer focused at Cartesian coordinates x_i, y_i, and z_i is given by[3]

$$\hat{m}(x_i, y_i, z_i, \omega_0) = \frac{\mathbf{w}(x_i, y_i, z_i, \omega_0)^{\mathrm{H}} \, \mathbf{R}(\omega_0) \, \mathbf{w}(x_i, y_i, z_i, \omega_0)}{\mathbf{w}(x_i, y_i, z_i, \omega_0)^{\mathrm{H}} \, \mathbf{w}(x_i, y_i, z_i, \omega_0)}, \tag{1}$$

where $\mathbf{R}(\omega_0)$ is the N-by-N normalized CSDM and the superscript "H" is the matrix complex conjugate transpose.

The CSDM matrix is normalized to offset the effects of channel-to-channel amplitude discrepancies in the human data. Although the array used to acquire the data can be calibrated in the laboratory, previous experience has shown that the calibrations change moderately when the array is placed in the intercostal region of a human. The normalization, which helps to moderate the effect of the changing calibration, is based on a vector of the diagonal elements of the unnormalized CSDM $\overline{\mathbf{R}}(\omega_0)$, where $\overline{\mathbf{R}}(\omega_0) = \mathrm{E}[\mathbf{x}(\omega_0)\, \mathbf{x}(\omega_0)^{\mathrm{H}}]$ and E[ ] is the statistical expectation operator. This vector of diagonal elements, $\overline{R}_{ii}(\omega_0)$ (for $1 \le i \le N$), is expressed as

$$\mathbf{p}(\omega_0) = \begin{bmatrix} \sqrt{\overline{R}_{11}(\omega_0)} \\ \sqrt{\overline{R}_{22}(\omega_0)} \\ \\ \vdots \\ \\ \sqrt{\overline{R}_{NN}(\omega_0)} \end{bmatrix}, \tag{2}$$

where N is the number of sensors used to acquire data and the bar denotes the unnormalized CSDM. With this vector, a matrix can be computed by using the outer product of the vector with itself as

$$\mathbf{P}(\omega_0) = \mathbf{p}(\omega_0)\mathbf{p}^{\mathrm{H}}(\omega_0) \, . \tag{3}$$

Once $\mathbf{P}(\omega_0)$ is known, the entries of the CSDM can be individually normalized with the equation

$$R_{ij}(\omega_0) = \frac{\overline{R}_{ij}(\omega_0)}{P_{ij}(\omega_0)} \, , \tag{4}$$

where the subscripts i and j denote the individual entries by row and column, respectively.

For the so-called RVDR focused beamformer, $\mathbf{w}(x_i, y_i, z_i, \omega_0)$ is defined as

$$\mathbf{w}(x_i, y_i, z_i, \omega_0) = \hat{\mathbf{R}}(\omega_0)^{-1} \, \mathbf{d}(x_i, y_i, z_i, \omega_0) \, . \tag{5}$$

In equation (5), $\mathbf{d}(x_i, y_i, z_i, \omega_0)$ is the N-by-1 focusing vector with the nth element given by

$$d_n(x_i, y_i, z_i, \omega_0) = \frac{1}{[r_i(n)]^{\beta}} \exp\left[\frac{\mathrm{j}\omega_0 r_i(n)}{c}\right], \tag{6}$$

where β is a geometric spreading loss factor, c is the average shear wave speed in the medium, and $r_i(n)$ is the apparent Euclidean distance from the ith image point to the nth sensor located at $x(n)$, $y(n)$, and $z(n)$ expressed as

$$r_i(n) = \sqrt{[x_i - x(n)]^2 + [y_i - y(n)]^2 + [z_i - z(n)]^2} \ . \tag{7}$$

The diagonal-enhanced CSDM $\hat{\mathbf{R}}(\omega_0)$ is defined by

$$\hat{\mathbf{R}}(\omega_0) = \mathbf{R}(\omega_0) + e\left\{\frac{\text{Trace}\left[\mathbf{R}(\omega_0)\right]}{N}\right\}\mathbf{I} \ , \tag{8}$$

where e is the scalar enhancement factor and $\mathbf{I}$ is the N-by-N identity matrix. It is noted that as e approaches infinity, equation (1) becomes a CFB, and as e approaches zero, equation (1) becomes a minimum variance distortionless response (MVDR) beamformer. In addition, the image scalar pixel value of the CFB at Cartesian coordinates x_i, y_i, and z_i can be written in simplified form as[3]

$$\hat{c}(x_i, y_i, z_i, \omega_0) = \frac{\mathbf{d}(x_i, y_i, z_i, \omega_0)^{\mathrm{H}} \, \mathbf{R}(\omega_0) \, \mathbf{d}(x_i, y_i, z_i, \omega_0)}{\mathbf{d}(x_i, y_i, z_i, \omega_0)^{\mathrm{H}} \, \mathbf{d}(x_i, y_i, z_i, \omega_0)} \ , \tag{9}$$

where the elements of $\mathbf{d}(x_i, y_i, z_i, \omega_0)$ are shown in equation (6).

3. EXPERIMENT

All the measurements in this report were taken with a one-dimensional array that consists of 14 equally spaced sensors (elements). The element-to-element midpoint spacing between adjacent sensors is 0.00635 m (0.250 in.), as shown in figure 2. A coordinate system is chosen such that the primary axis is the x-axis. The y-axis is the image depth into the medium, which is the human thorax. The sensing elements of the array are polyvinylidene fluoride (PVDF) film strips that are 0.0159 m (0.625 in.) long and approximately 0.00610 m (0.240 in.) wide. Attached to the middle of each strip is a square piece of plastic, which has a 0.00267-m (0.105-in.) length and a 0.00127-m (0.050-in.) approximate thickness. The array elements were directly connected to individual preamplifiers located on the top of the array chassis.

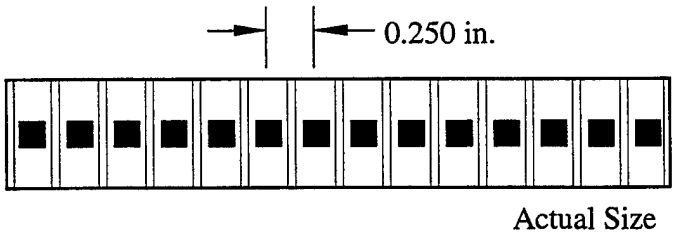

Figure 2. Fourteen-Channel Linear Array

The outputs from the array preamplifiers were connected to a 16-channel low-noise amplifier system with coaxial cables. The signals were passed to a bank of amplifiers (Ithaco Model 451) with the low-frequency (single-pole) rolloff set to 1000 Hz, which provided attenuation of the signals in the 0- to 100-Hz frequency range. The signals then traveled to a multichannel programmable (16-pole) filter (Precision Filter), with the high-frequency cutoff set to 800 Hz, which attenuated the signal content above 800 Hz. Finally, the signals were passed to a data acquisition system (LabView) residing in a computer (Apple Power Macintosh 8100/110), where the time series data were stored for post-acquisition processing.

The human data were collected with the subject in an anechoic, electromagnetic (EM) shielded room. The subject was chosen because of access to a previously acquired angiogram and the accessibility of the attending cardiologist. In this particular case, the coronary artery system includes the median ramus (or trifurcation). With the subject positioned chest up on a hammock suspended with bungee cords, tests were conducted on 3 November 1997, just 5

months after a stent implantation in the LAD artery just below the circumflex coronary artery branch. The array was placed in the fourth intercostal space on the left-hand side of the body (the region below the coronary artery triple-branching point (trifurcation)), which would ensure that the area around the LAD was being imaged. Two minutes of data were taken, and the resulting time series files were edited by extracting about one-tenth of a second of data in the middle of each diastolic phase and concatenating these segments together into an edited file. This file was then transformed into the frequency domain with a time sequence of 48 nonoverlapping fast Fourier transforms, each containing 256 time sample points. The frequency domain data had a spectral bin width of 7.9 Hz. Once the CSDM was formed from a time average of the 14-by-14 matrix $\mathbf{x}(\omega_0)\,\mathbf{x}(\omega_0)^{\mathrm{H}}$, the beamformers were applied to produce the images.

Figures 3, 4, 5, 6, 7, and 8 are RVDR images of the subject at 157.5, 299.3, 441.0, 582.8, 614.3, and 779.7 Hz, respectively, with the scalar enhancement factor (e) set to 0.01. The wave speed used to process the data is a soft tissue shear wave dispersion curve.[4] As previously discussed, the y-axis is depth into the image volume (cm), and the x-axis is the dimension along the axis of the array (cm), with $x = 0$ corresponding to the center of the array. Each figure has the following characteristics: the image is computed at $z = 0$; the individual sensors of the array are denoted with a yellow rectangle; the image scale is normalized decibels with a maximum value of zero dB; and the color scale is to the right of the plot. The normalization factors of the images are listed in table 1.

The most prominent detail of the images is seen in the red ridge of energy that runs nominally from x = -1 and y = 10 down into the image to about y = 3 cm. Based on these experimental images and the simulations in section 4, it has been concluded that this energy emanates from the vicinity of the LAD artery. The image resolution is sufficient to determine its origin with respect to the x-axis span of the array; however, it is not adequate for depth resolution. This process of localization and identification is discussed more thoroughly in section 5. Note that image resolution increases as frequency increases.

Figures 9, 10, 11, 12, 13, and 14 are CFB images of the subject at 157.5, 299.3, 441.0, 582.8, 614.3, and 779.7 Hz, respectively. Although no image details are resolvable, the CFB processing is included in this report to allow comparisons with the simulations and to indicate the necessity for a high-resolution minimum variance focused beamforming operation.

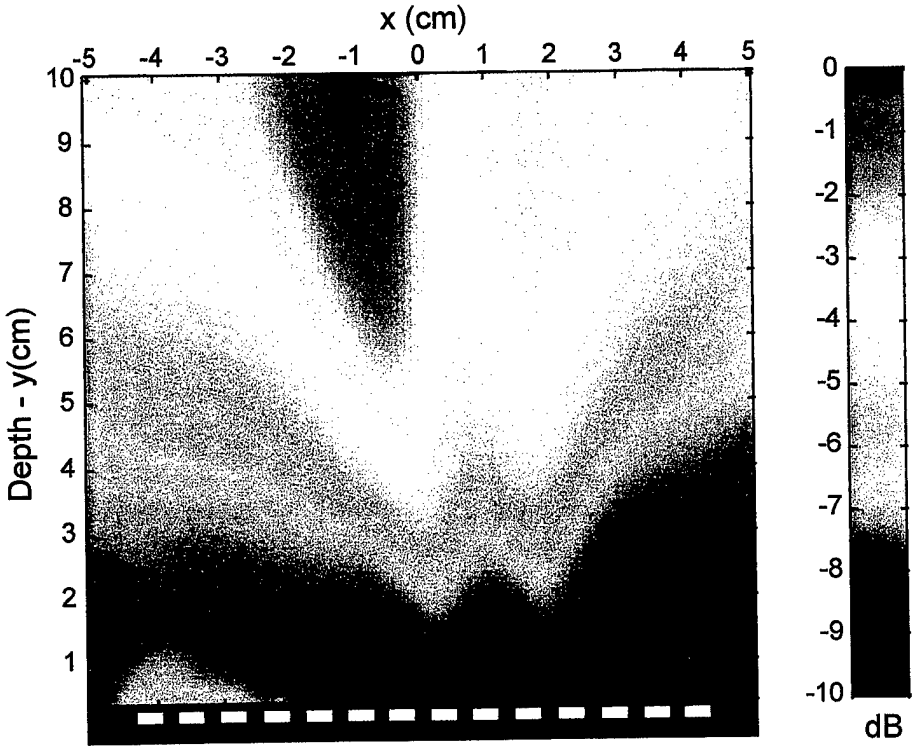

Figure 3. RVDR for Experimental Data at 157.5 Hz

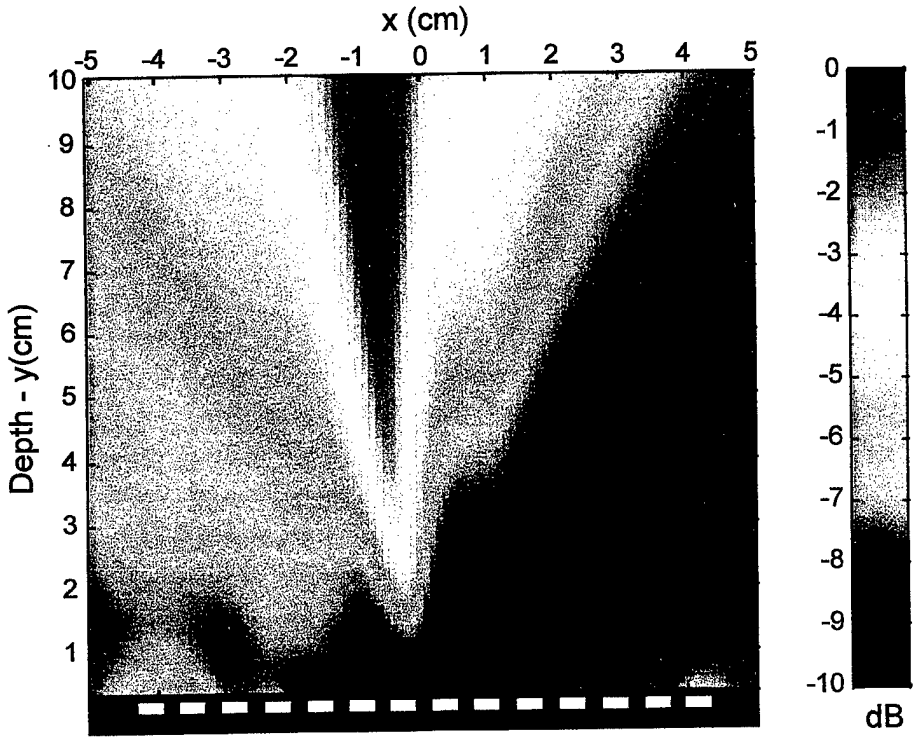

Figure 4. RVDR for Experimental Data at 299.3 Hz

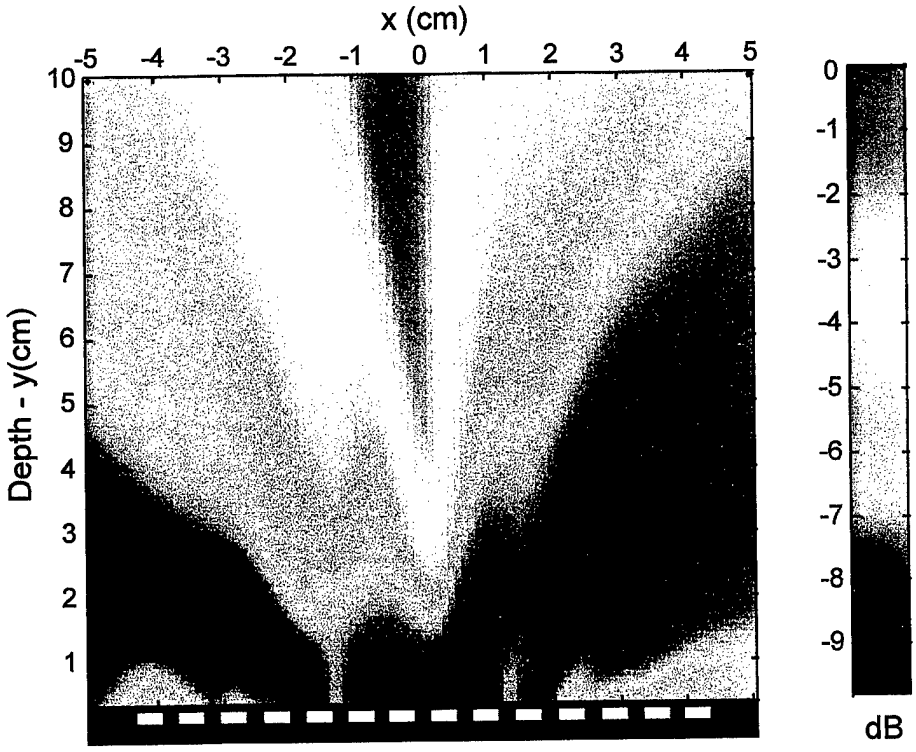

Figure 5. RVDR for Experimental Data at 441.0 Hz

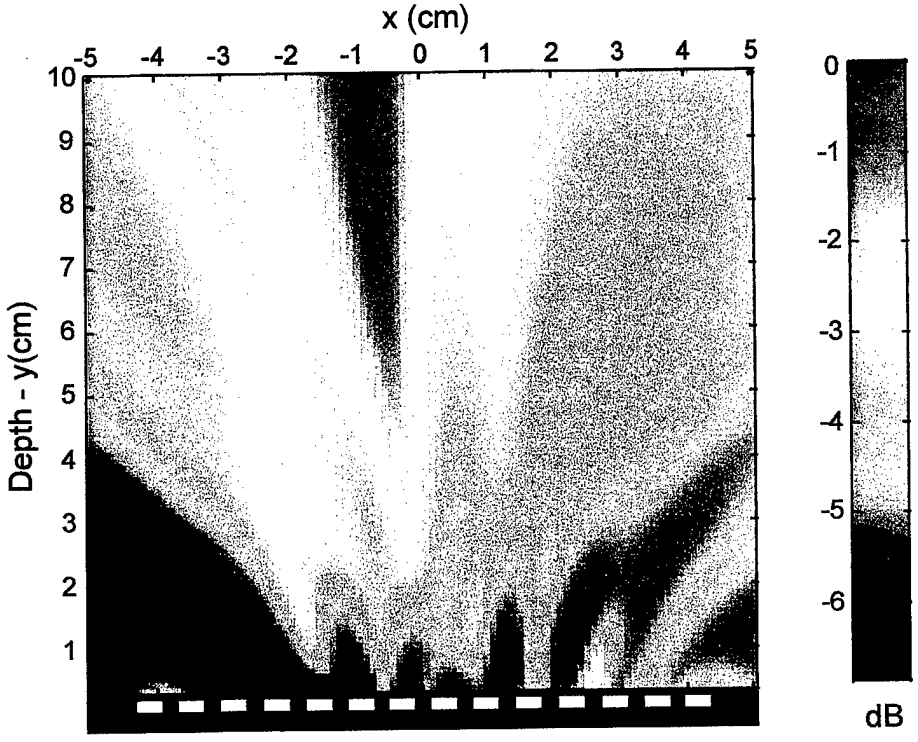

Figure 6. RVDR for Experimental Data at 582.8 Hz

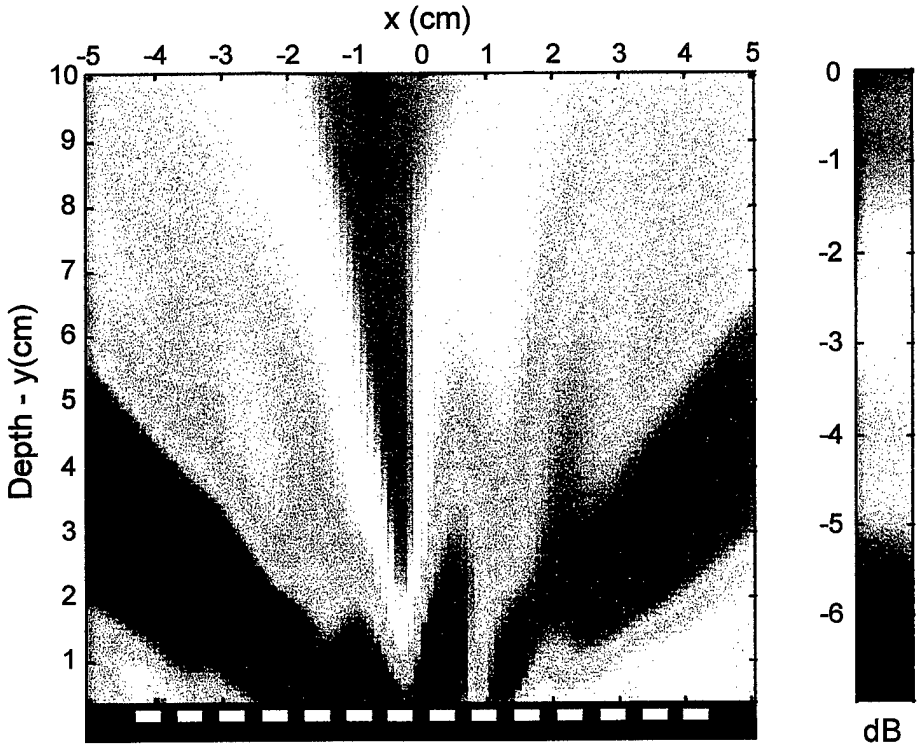

Figure 7. RVDR for Experimental Data at 614.3 Hz

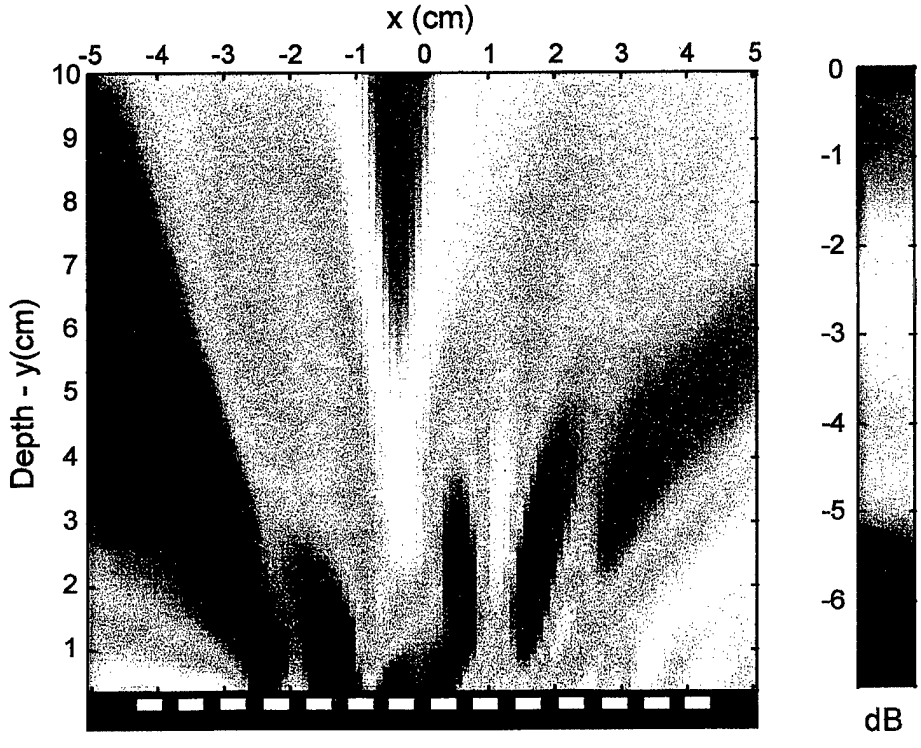

Figure 8. RVDR for Experimental Data at 779.7 Hz

Table 1. Image Normalization Factors in Decibels for the Experiment

Frequency (Hz)	RVDR	CFB
157.5	-11.3	8.5
299.3	-9.1	7.1
441.0	-7.7	5.7
582.8	-7.8	5.3
614.3	-8.6	5.1
779.7	-9.3	5.1

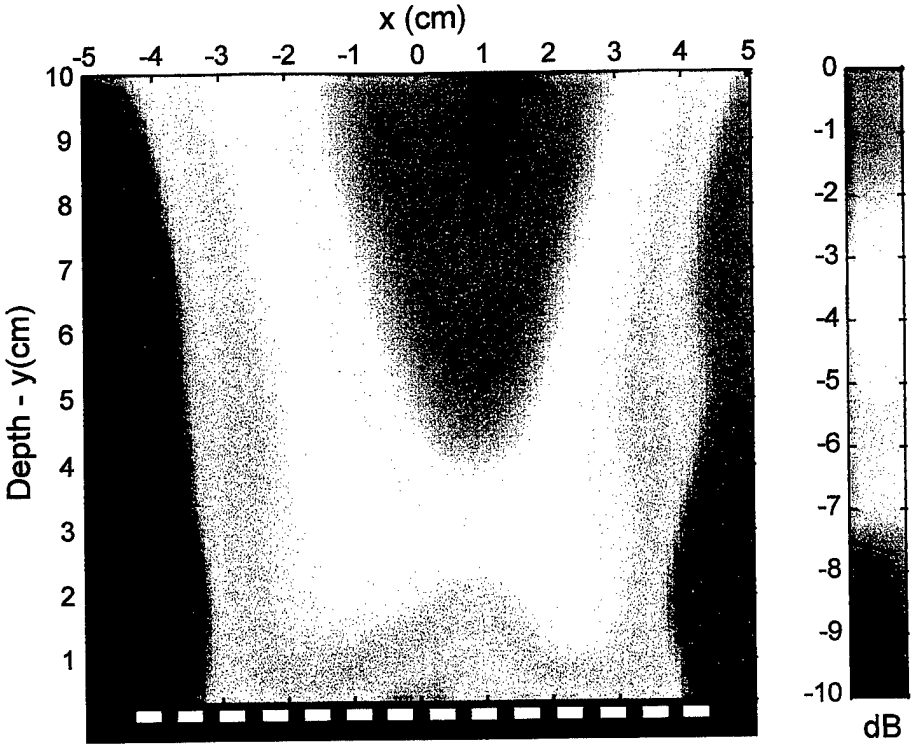

Figure 9. CFB for Experimental Data at 157.5 Hz

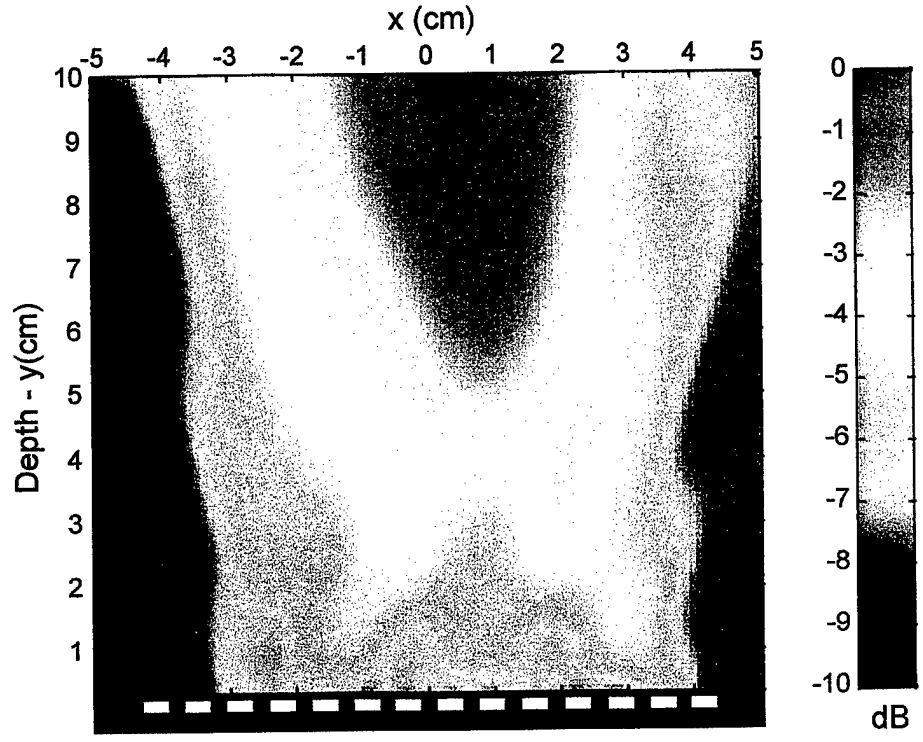

Figure 10. CFB for Experimental Data at 299.3 Hz

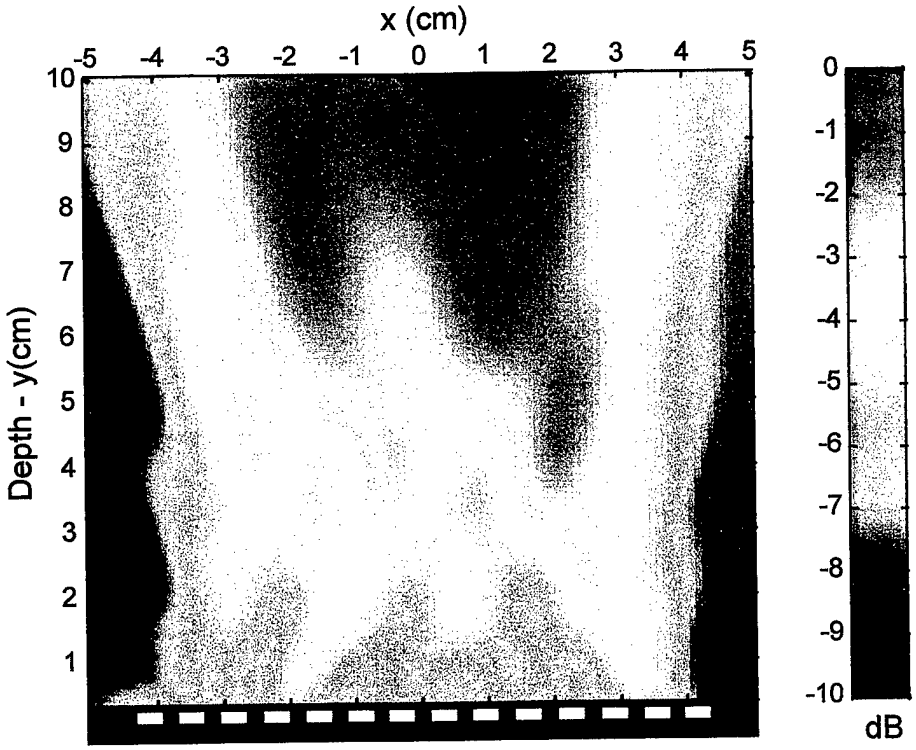

Figure 11. CFB for Experimental Data at 441.0 Hz

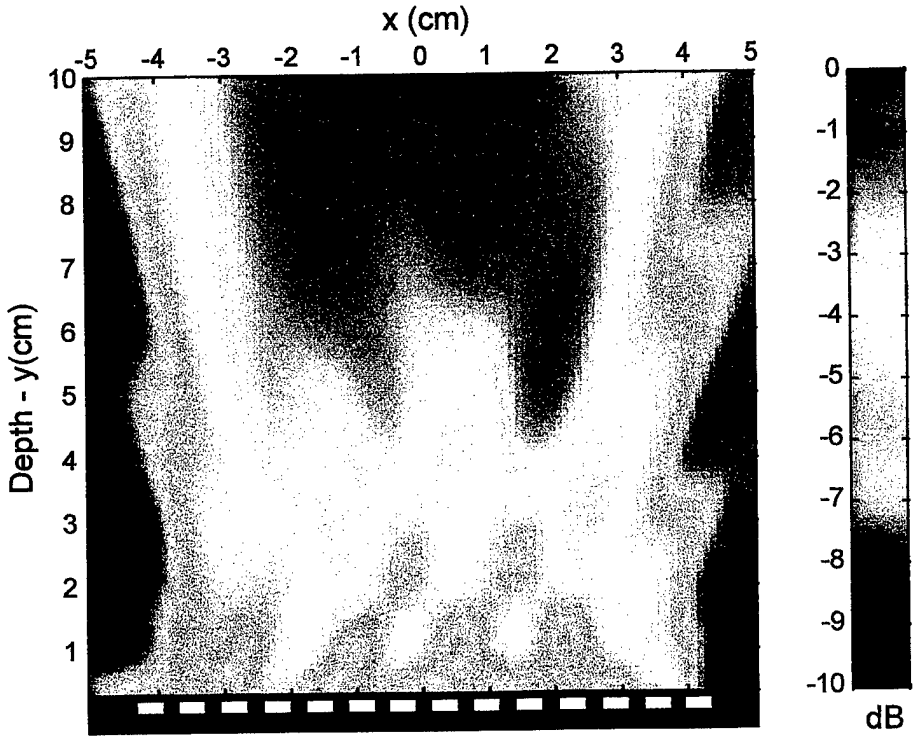

Figure 12. CFB for Experimental Data at 582.8 Hz

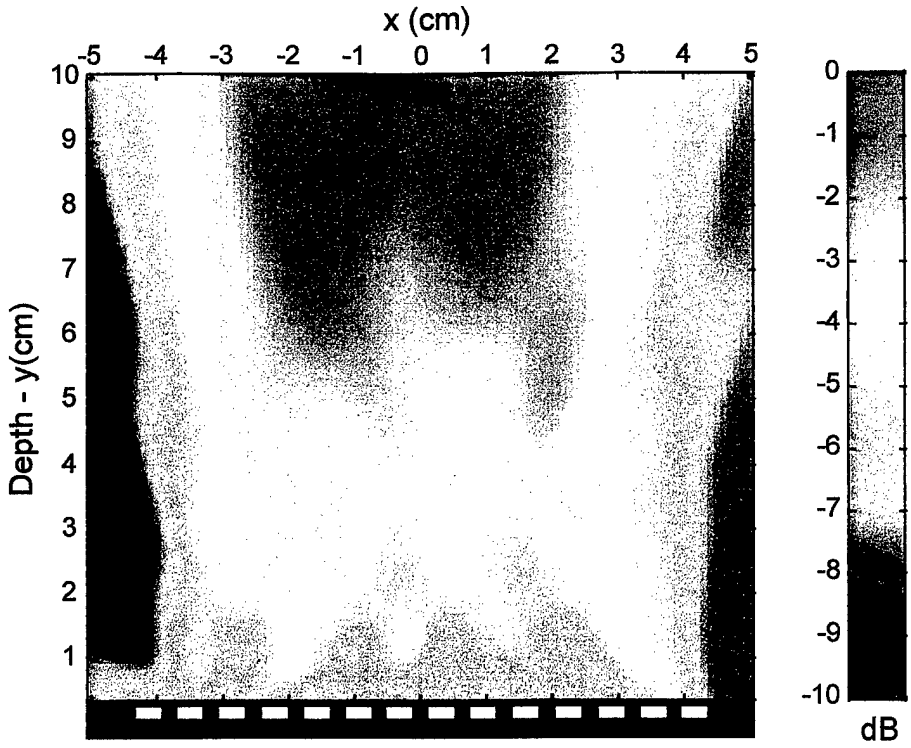

Figure 13. CFB for Experimental Data at 614.3 Hz

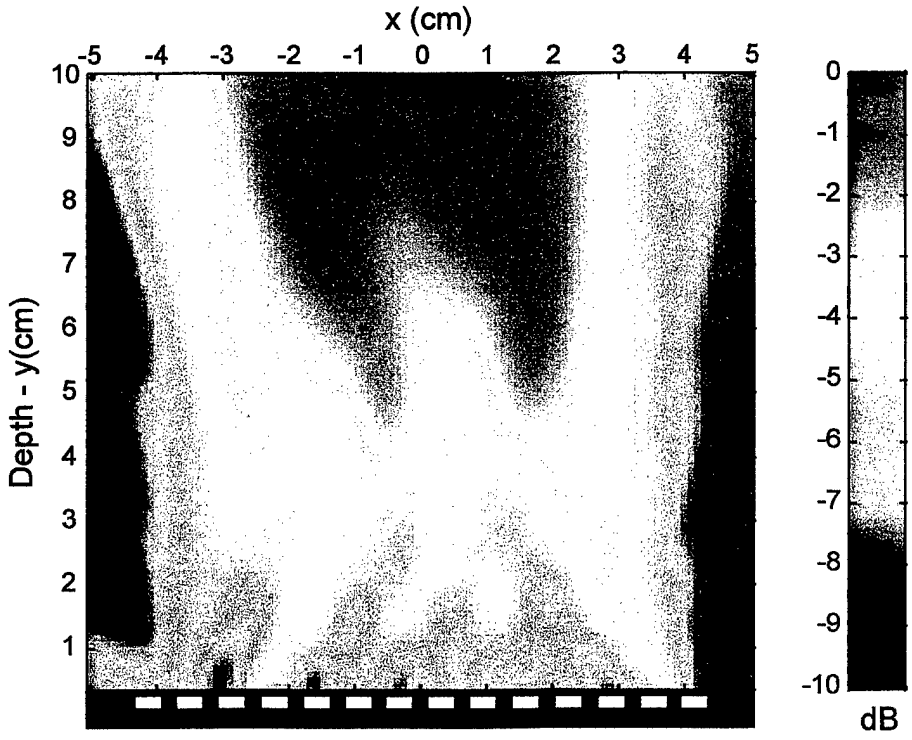

Figure 14. CFB for Experimental Data at 779.7 Hz

4. SIMULATION

Numerical simulations of the LAD artery imaging problem consist of analytically modeling the CSDM, inserting it into equations (1) and (9), and then calculating the simulated beamformed image. Several different geometric configurations that correspond to human LAD artery anatomy are modeled and discussed below. Comparisons of simulated data to human data are discussed later in the report.

As mentioned previously, the images of the human data were produced during the diastolic phase of the heart cycle. The diastolic phase represents the part of the cycle where blood flow through the coronary arteries is at a maximum rate. This type of flow-derived kinetic energy (in a diseased artery) can be modeled (1) when the flow is at an elevated Reynolds number and has become turbulent or (2) when the mass volume of the blood traveling down the artery is exciting a (mechanical) propagating wave in the wall of the artery itself. Either mechanism will transmit energy into the surrounding soft tissue, although turbulent flow is nearly spatially uncorrelated and mechanical wave energy is highly correlated. Both types of energy are modeled as a linear source.

Additionally, during the diastolic phase, blood in the atrium is flowing through the bicuspid (left) mitral valve and the tricuspid (right) valve into the corresponding ventricles. This produces forces against the inside of the heart wall that result in both compression and shear wave energy propagation, resulting, in turn, in motion on the surface of the heart, specifically outside the left and right ventricles and on the interventricular groove. This type of flow-induced energy is highly coherent over the surface and accordingly the heart wall is modeled as a planar source. These same forces also produce motion in the septum, which is at a lower power level than that at the front heart wall due to the force balance on each side of the septum. The septum is modeled similarly to the front heart wall. Each planar and linear source is modeled first individually and then together, so as to understand both its singular effects and its interaction with the other sources.

4.1. A SINGLE NEARLY UNCORRELATED LINE SOURCE

The first simulation is that of a single nearly spatially uncorrelated line source. This case arises when turbulent flow through a small-diameter tube causes an energy distribution with a uniform power spectrum that transmits energy into the surrounding medium. The model of the line source is 0.102 m (4 in.) long, and it is discretized using $M = 65$ spherical

energy radiators that are placed in a line with a 0.00159-m (0.0625-in.) spacing between each. An intersource correlation matrix is added to the model to account for the effective spatial coherence of the turbulent flow-induced motion at the tube interface with the surrounding medium. Note, however, that the correlation distance of turbulent flow is extremely short, and thus the simulation is entitled "nearly uncorrelated."

The expression for the streamwise wall pressure autospectrum is given as[5]

$$P(x,\omega_0) = p(x)\exp\left(\frac{-\gamma \mid x \mid \omega_0}{U_c}\right)\exp\left(\frac{j\omega_0 x}{U_c}\right), \tag{10}$$

where $p(x)$ is the amplitude of the wall pressure, x is the streamwise location of the flow measured from a single reference point (m), γ is the spatial decay constant (dimensionless), and U_c is the fluid convection speed (m/s). For this study, the spatial decay constant was 0.125 and the fluid convection speed was 2.50 m/s, which is the minimum flow rate for turbulent blood in a coronary artery. (Turbulent blood as an energy source is further discussed later in this report.)

Equation (10) is used to form the M-by-M intersource CSDM $\mathbf{E}(\omega_0)$ for the multiple point sources of the composite linear source. In equations (11) and (12), $\mathbf{E}(\omega_0)$ has the element in the uth row and vth column given by

$$E_{uv}(\omega_0) = \begin{cases} \exp\left(\dfrac{-\gamma|x_u - x_v|\omega_0}{U_c}\right)\exp\left(\dfrac{j\omega_0(x_u - x_v)}{U_c}\right), & u < v \\ 1, & u = v \\ \exp\left(\dfrac{-\gamma|x_u - x_v|\omega_0}{U_c}\right)\exp\left(\dfrac{j\omega_0(x_v - x_u)}{U_c}\right), & v < u \end{cases}. \tag{11}$$

For the source model used here, the indices u and v range from 1 to 65. Implicit in equation (11) is the source level $p(x)$, which has been normalized to unity at all locations. Once this intersource matrix is known, the simulated CSDM can be determined using

$$\mathbf{R}(\omega_0) = \sigma_s^2 \left\{ \frac{N}{\text{Trace}\left[\mathbf{D}(\omega_0)\,\mathbf{E}(\omega_0)\,\mathbf{D}^{\mathrm{H}}(\omega_0)\right]} \right\} \mathbf{D}(\omega_0)\,\mathbf{E}(\omega_0)\,\mathbf{D}^{\mathrm{H}}(\omega_0) + \sigma_0^2 \mathbf{I}\,, \tag{12}$$

where $\mathbf{D}(\omega_0)$ is the N-by-M matrix of propagation response vectors with the nu^{th} element given by

$$D_{nu}(\omega_0) = \frac{1}{[l(n,u)]^{\beta}} \exp\left[\frac{\mathrm{j}\omega_0\, l(n,u)}{c}\right], \tag{13}$$

where $l(n,u)$ is the Euclidean distance from the nth sensor to the uth source, given as

$$l(n,u) = \sqrt{[x(n)-x(u)]^2 + [y(n)-y(u)]^2 + [z(n)-z(u)]^2}\,. \tag{14}$$

The spectral density of the zero-mean, spatially uncorrelated additive noise at each sensor is σ_0^2, and the signal at the peak of the spatial spectrum is σ_s^2.

The array sensors are assumed to be point sensors that measure normal displacement. The modeled geometry is shown in figure 15, where the line source is orthogonal to the linear array and offset from the middle of the array, such that x = -0.00635 m (-0.25 in.) for all points in the linear source. The depth of the line source is 0.0318 m (1.25 in.), which is the minimum distance from the chest wall to the LAD artery in an average human.[6]

The following values were used for the simulation: the autopower spectral density of the zero-mean, spatially uncorrelated additive noise at each sensor (σ_0^2) = 0.01, the signal at the peak of the spatial spectrum (σ_s^2) = 1, and the spreading constant $(\beta) = 1$. The value of the wave speed of the medium was interpolated between the low- and high-frequency shear wave speeds for human soft tissue.[4] At 100 Hz, a value of 3.75 m/s was used, and at 1000 Hz, a value of 13.0 m/s was used.

Figures 16, 17, 18, and 19 are RVDR images of the simulation at 50, 200, 400, and 600 Hz, respectively, with the scalar enhancement factor (e) set to 0.01. The y-axis is depth into the image volume (cm), and the x-axis is the dimension along the axis of the array (cm), with x = 0 corresponding to the center of the array. Each figure has the following characteristics: the image is computed at z = 0; the individual sensors of the array are denoted

with a yellow rectangle; the physical location of the line source is represented as a circle and additionally marked with an arrow tipped line; the scale of the image is normalized decibels; and the color scale is to the right of the plot. The normalization factor of the images are listed in table 2.

Note that image resolution increases as frequency increases. The most prominent detail of these figures is the nearly uncorrelated linear source orthogonal to the array that does not image as a small piece of energy; rather, the beamformer locates the energy as a spatially extended source in volume depth. This effect is due to the spatial ambiguity of a linear receiving array scanning a three-dimensional volume (which contains a linear source) when mapped into a two-dimensional beamformed image. The linear array can only measure radial distance from the array axis. Figures 20, 21, 22, and 23 are CFB images of the simulation at 50, 200, 400, and 600 Hz.

Note that the resolution of the CFB images (compared to the corresponding RVDR images) is not nearly as sharp, even though both are numerical simulations where all of the parameters in the beamformer are perfectly matched to the medium parameters. Experimental beamformed images using RVDR will not be as sharply resolved because of parametric mismatch. In addition, note that the line source is appearing as a spatially extended energy distribution, similar to that of the CFB image. The high-resolution signal processing algorithm also cannot resolve the spatial ambiguity effect, which renders the linear array incapable of discriminating between the true depth and the apparent depth for the elemental source component in the linear source, as shown in figure 24.

Table 2. Image Normalization Factors in Decibels for the First Simulation

Frequency (Hz)	RVDR	CFB
50.0	-5.8	11.3
200.0	-9.5	11.1
400.0	-10.1	10.9
600.0	-10.4	10.8

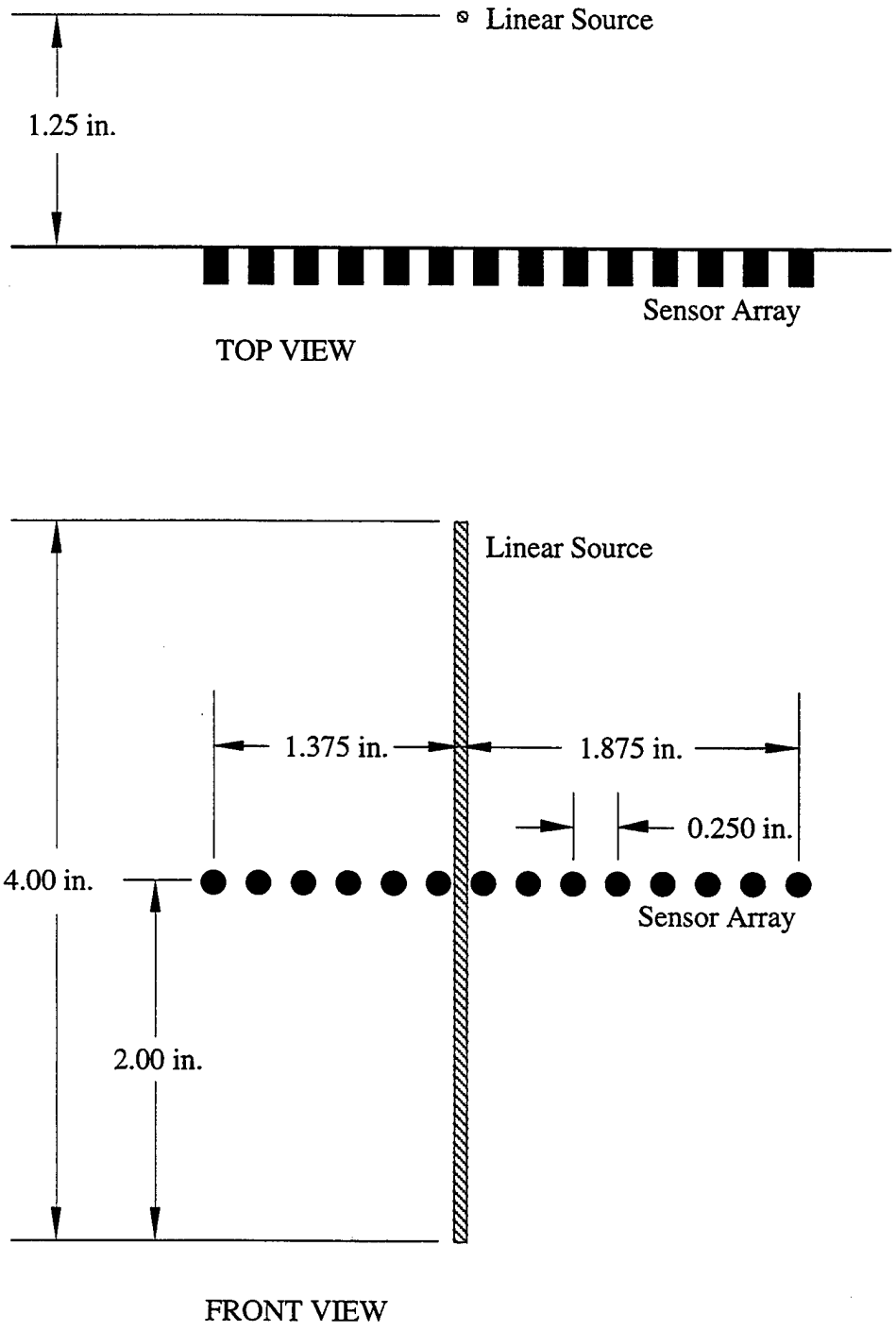

Figure 15. Geometry of the Simulations with a Single Linear Source

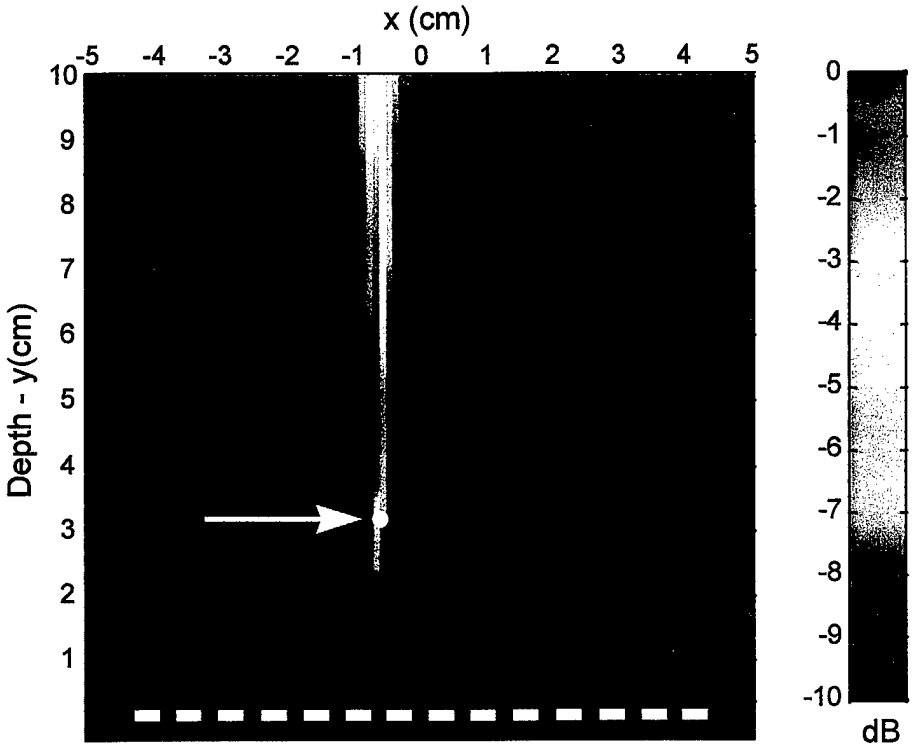

Figure 16. RVDR for Simulation One at 50 Hz

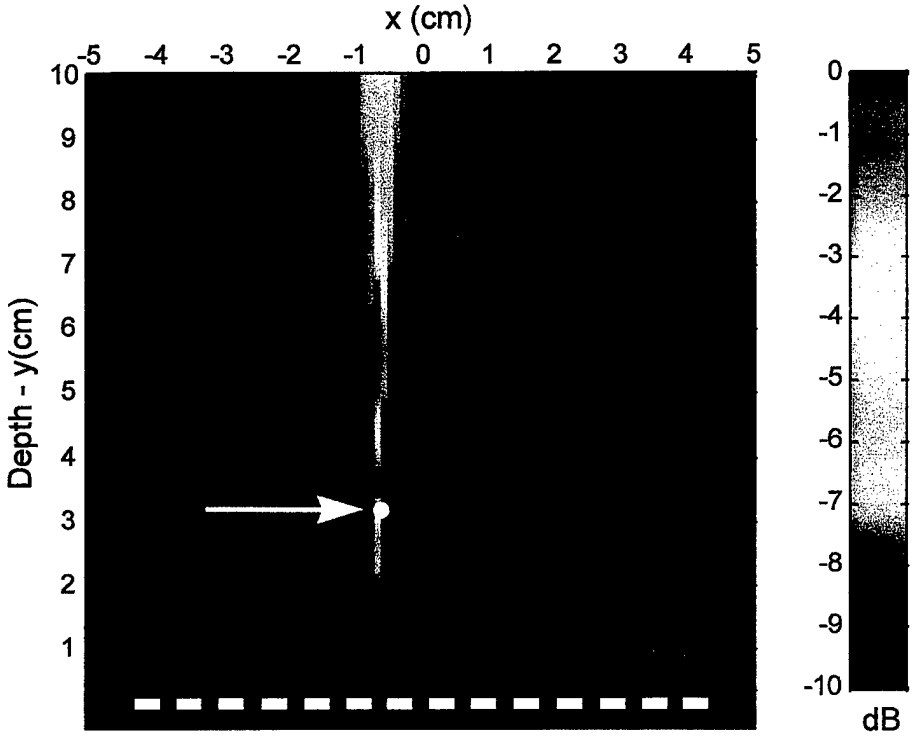

Figure 17. RVDR for Simulation One at 200 Hz

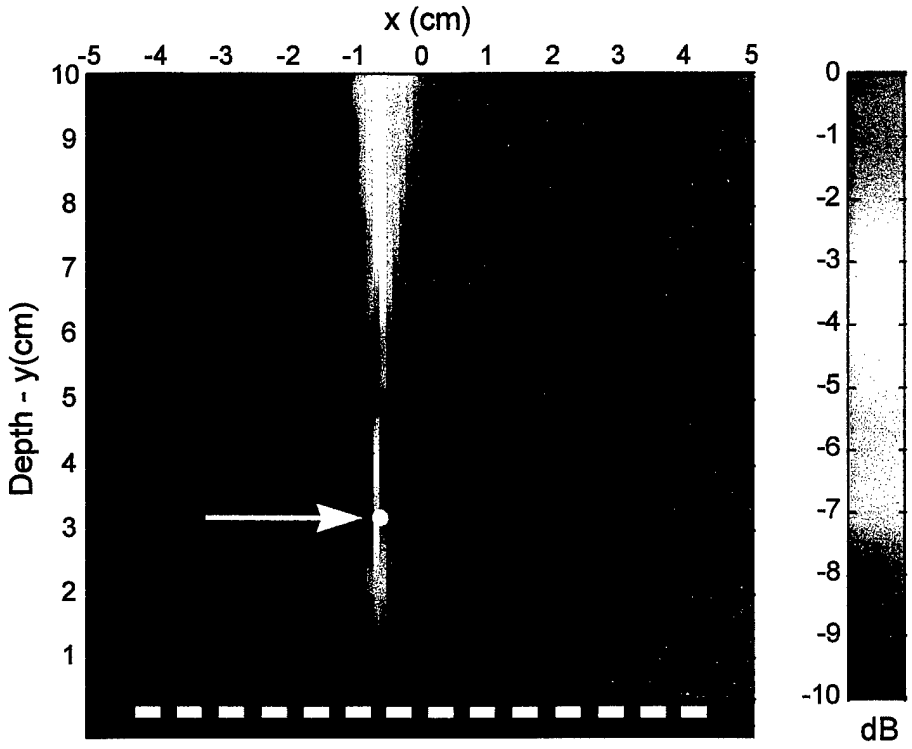

Figure 18. RVDR for Simulation One at 400 Hz

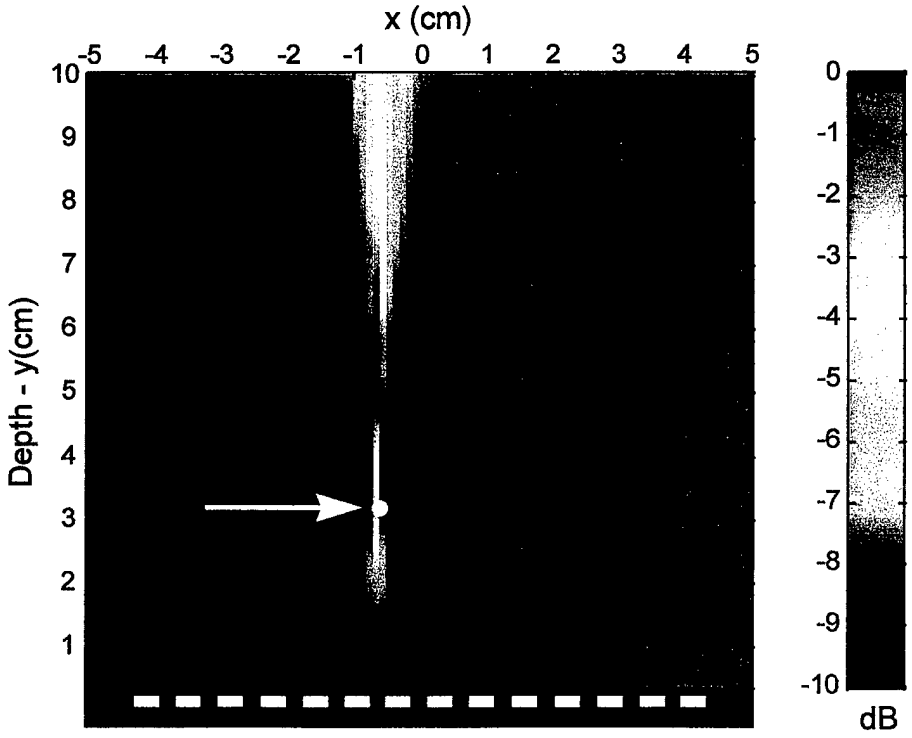

Figure 19. RVDR for Simulation One at 600 Hz

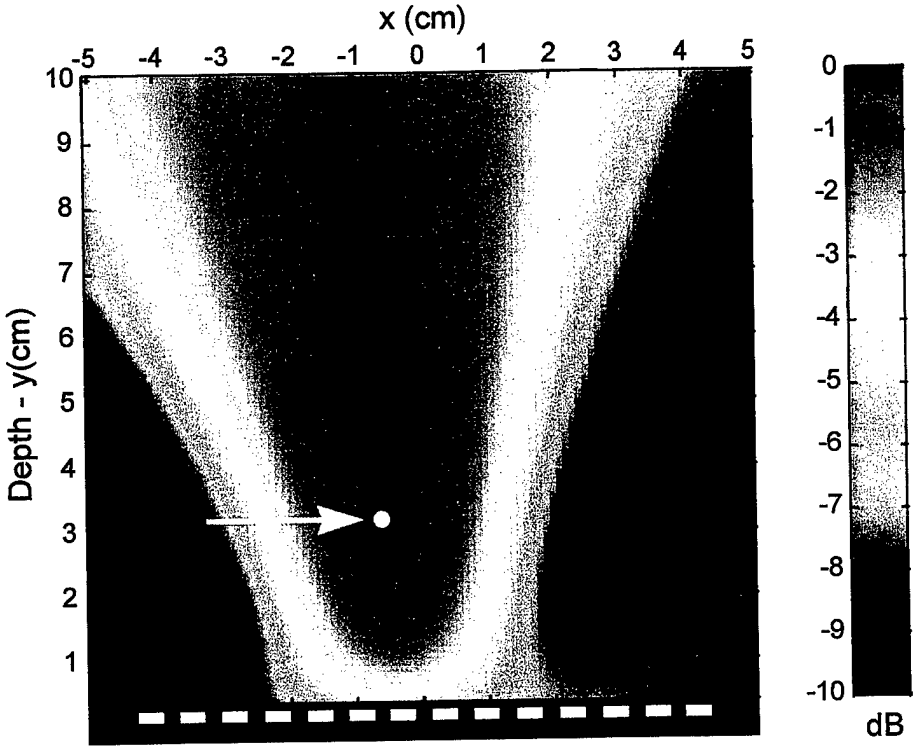

Figure 20. CFB for Simulation One at 50 Hz

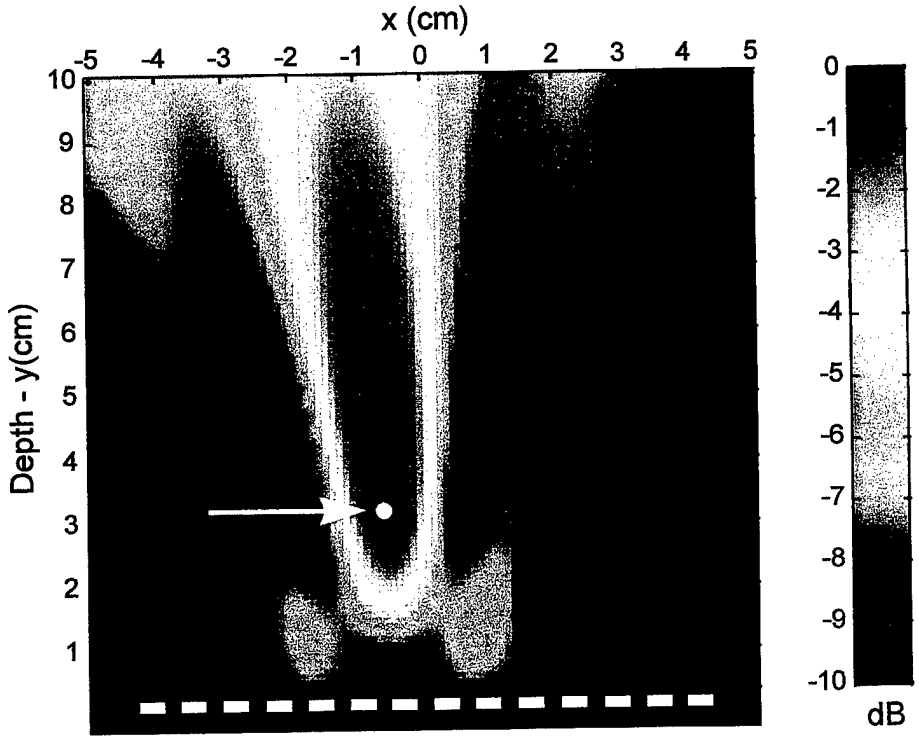

Figure 21. CFB for Simulation One at 200 Hz

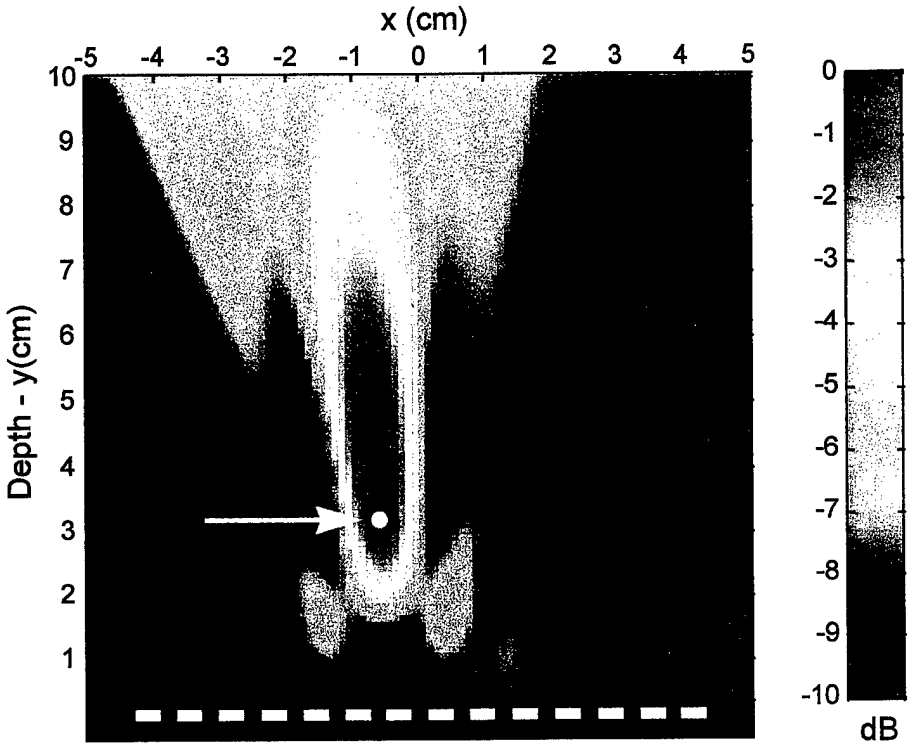

Figure 22. CFB for Simulation One at 400 Hz

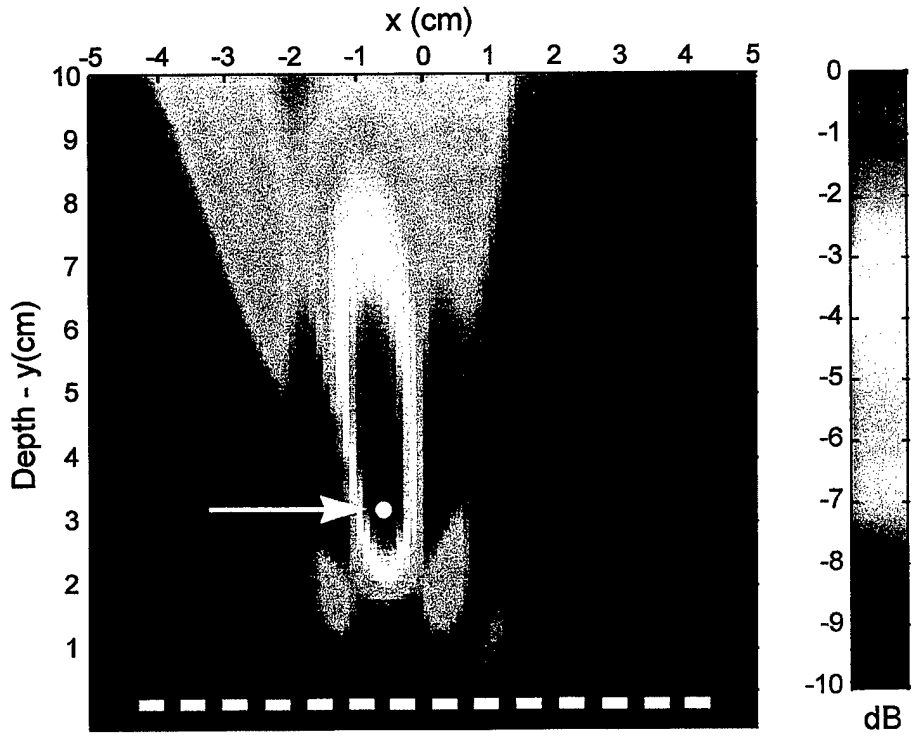

Figure 23. CFB for Simulation One at 600 Hz

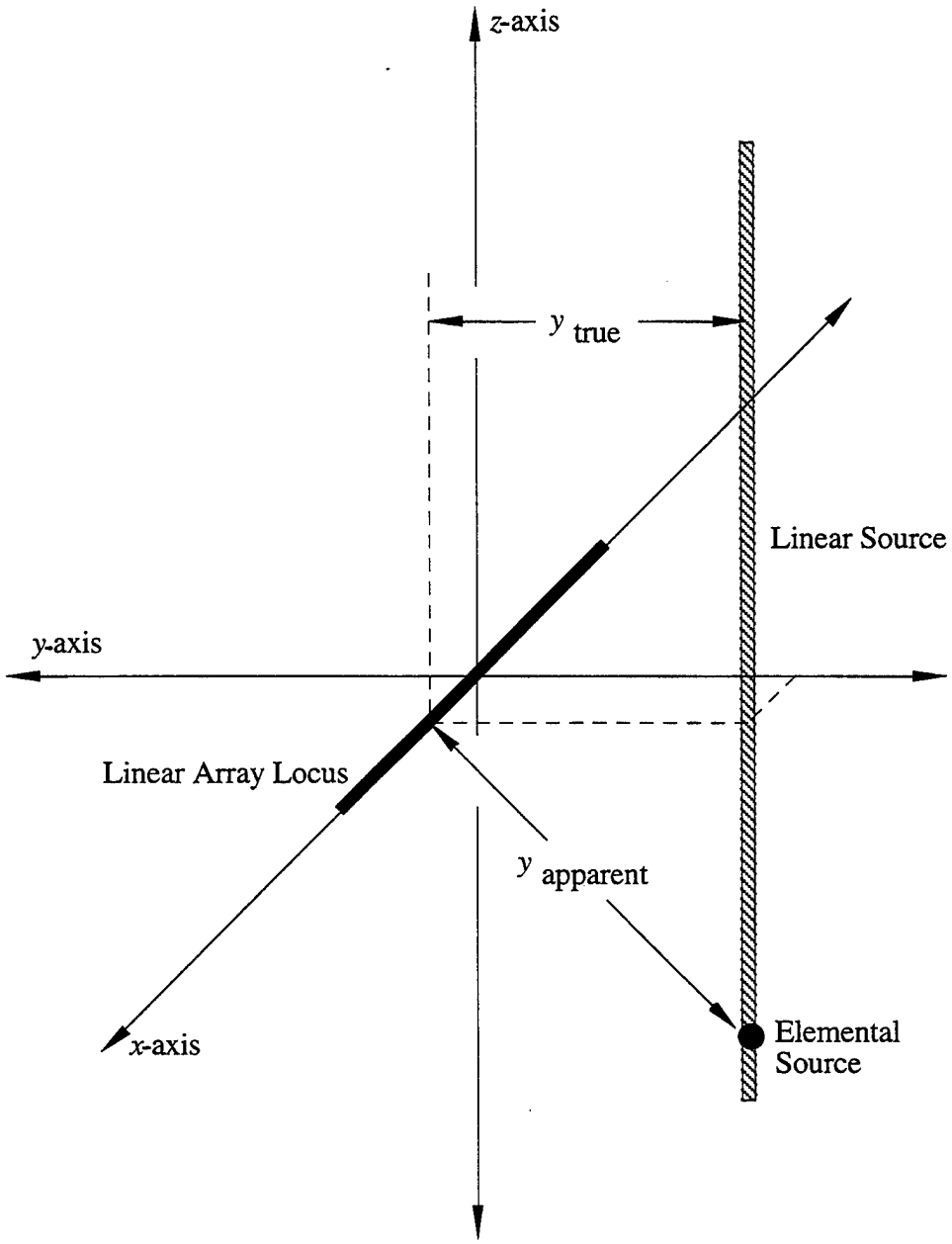

Figure 24. Source Depth Ambiguity with Linear Array and Orthogonal Linear Source

4.2. A SINGLE CORRELATED LINE SOURCE

The second simulation is that of a single correlated line source. This case arises when a propagating wave is excited in the wall of a small-diameter tube with a uniform power spectrum that transmits energy into the surrounding medium. The geometric configuration is identical to the first simulation. The only difference between simulation one and two is the *M*-by-*M* CSDM $\mathbf{E}(\omega_0)$ of the source, which has every element equal to unity, or

$$E_{uv}(\omega_0) = 1 \,, \tag{15}$$

indicating that each point source in the composite linear source is radiating in phase. Once the CSDM matrix of the source is known, the simulated CSDM is determined from equation (12). Figures 25, 26, 27, and 28 are RVDR images of the simulation at 50, 200, 400, and 600 Hz, respectively, with the scalar enhancement factor (e) set to 0.01. These figures are considerably different from corresponding figures 16-19 of simulation one. Although the detection of the main energy is similar, the dynamic range of the correlated simulation is much smaller than that of the nearly uncorrelated simulation. In the higher frequency images, the sidelobes are visible away from the main energy distribution. Additionally, large amounts of energy are appearing near the end of the array in all the correlated simulations. This "end effect" energy is an artifact of RVDR as it processes a correlated source. Figures 29, 30, 31, and 32 are CFB images of the simulation at 50, 200, 400, and 600 Hz, respectively. These figures are almost identical to corresponding figures 20-23 from simulation one. A slight difference is observed in the main energy area (shown in red), which is smaller for the second simulation. The normalization factors of the images are listed in table 3.

Table 3. Image Normalization Factors in Decibels for the Second Simulation

Frequency (Hz)	RVDR	CFB
50.0	-19.0	11.3
200.0	-17.2	11.3
400.0	-19.1	11.3
600.0	-19.7	11.2

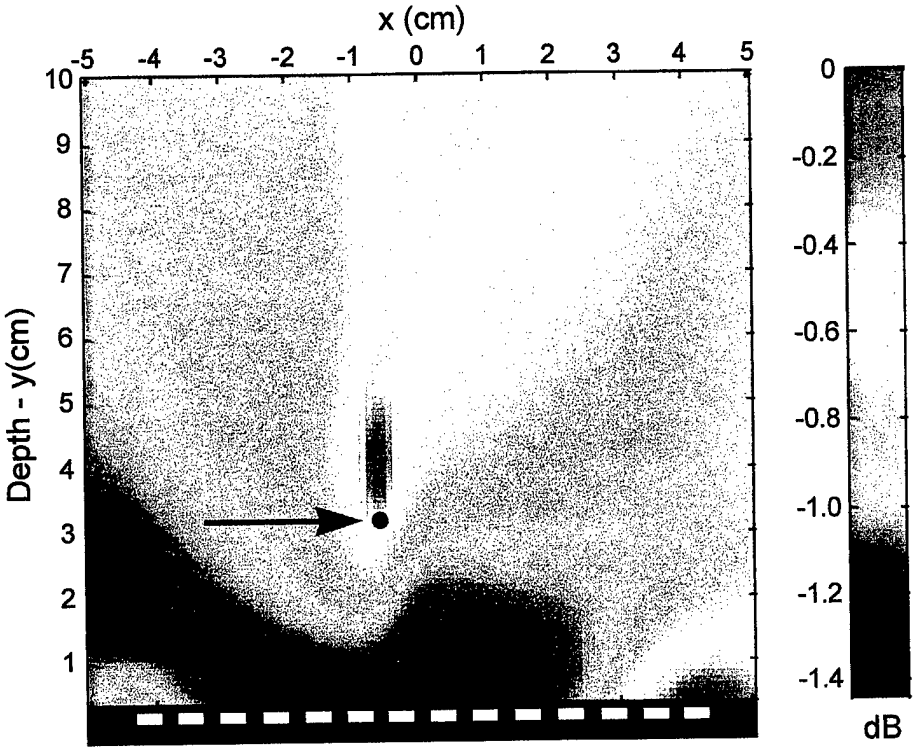

Figure 25. RVDR for Simulation Two at 50 Hz

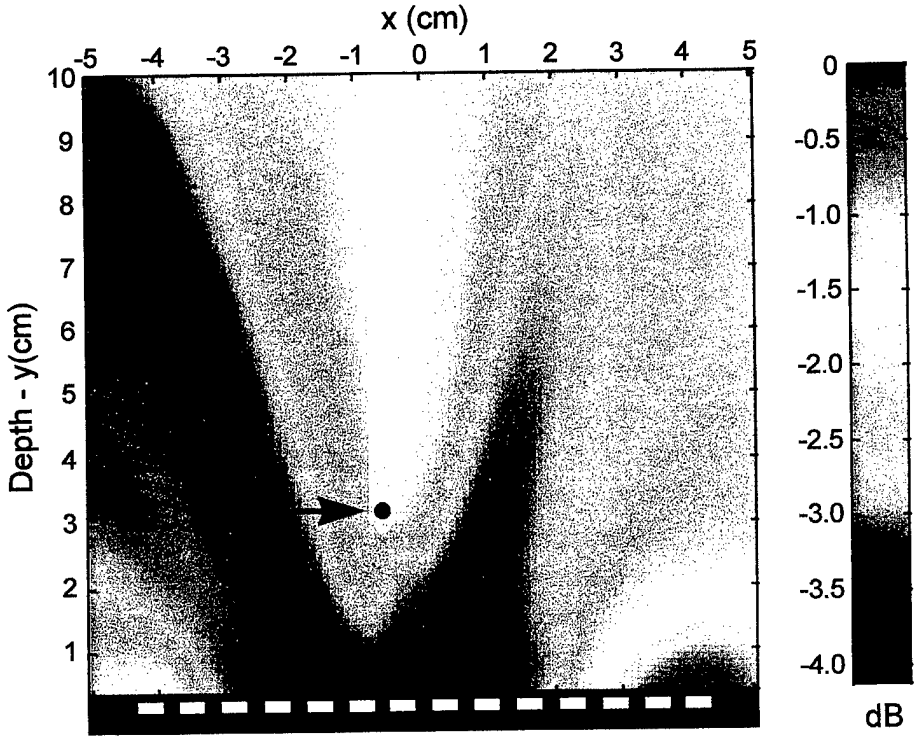

Figure 26. RVDR for Simulation Two at 200 Hz

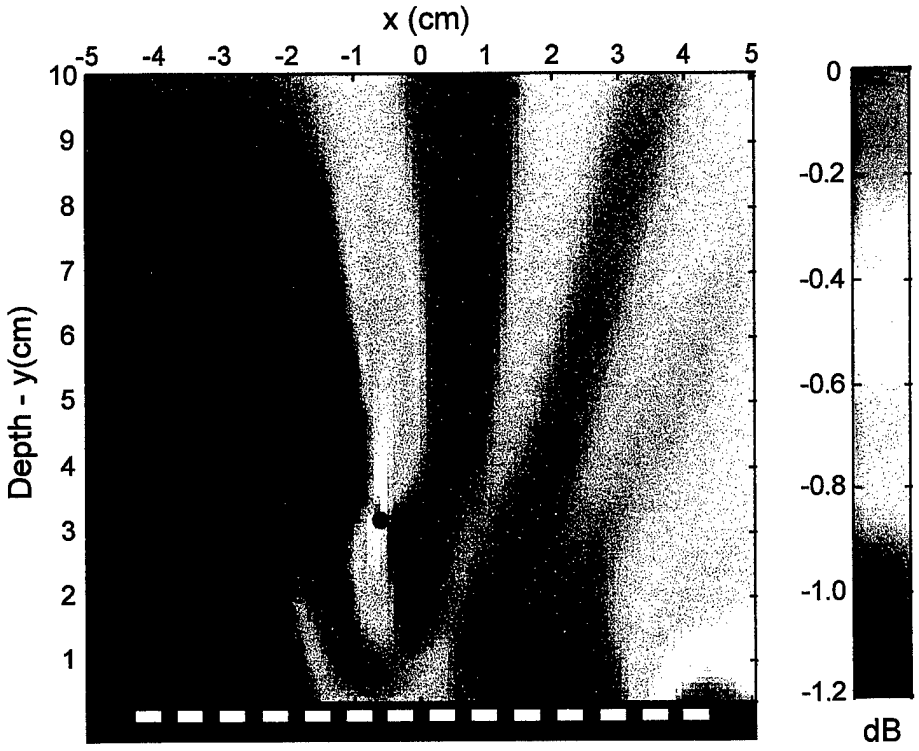

Figure 27. RVDR for Simulation Two at 400 Hz

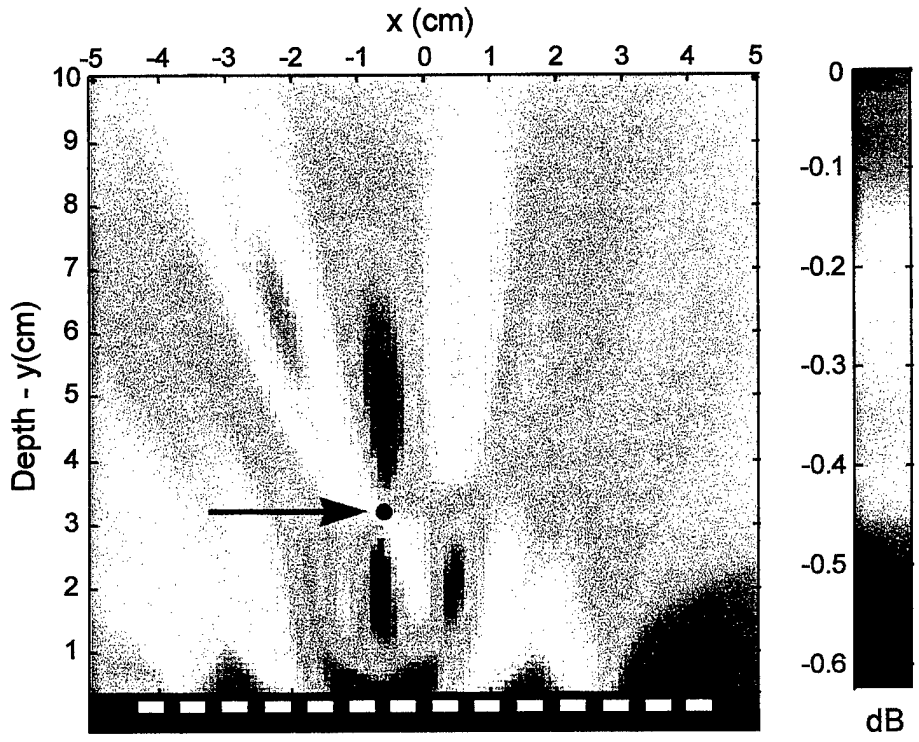

Figure 28. RVDR for Simulation Two at 600 Hz

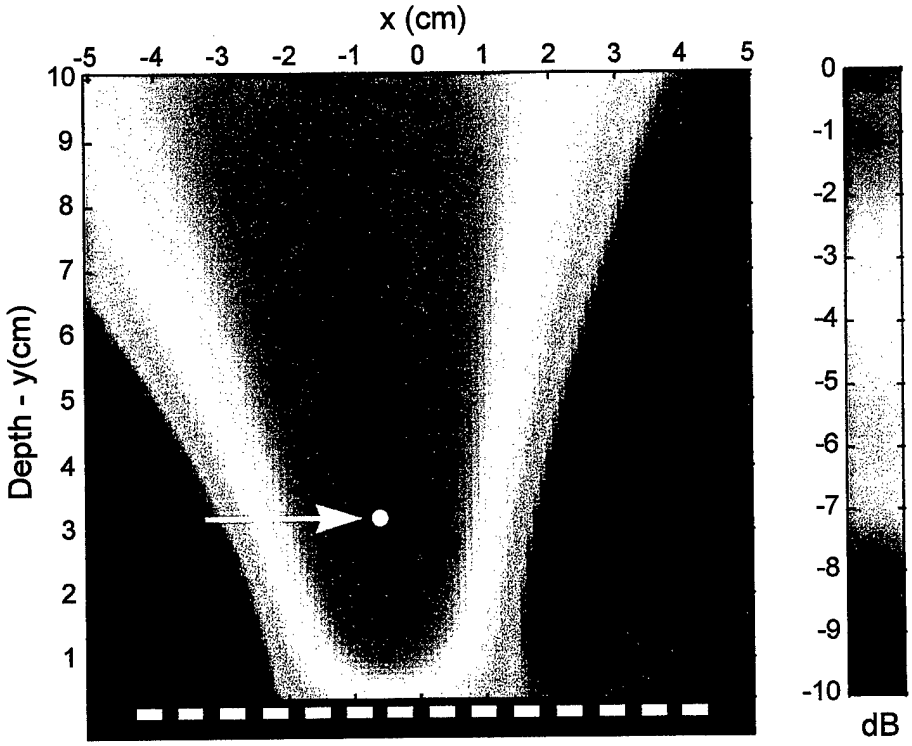

Figure 29. CFB for Simulation Two at 50 Hz

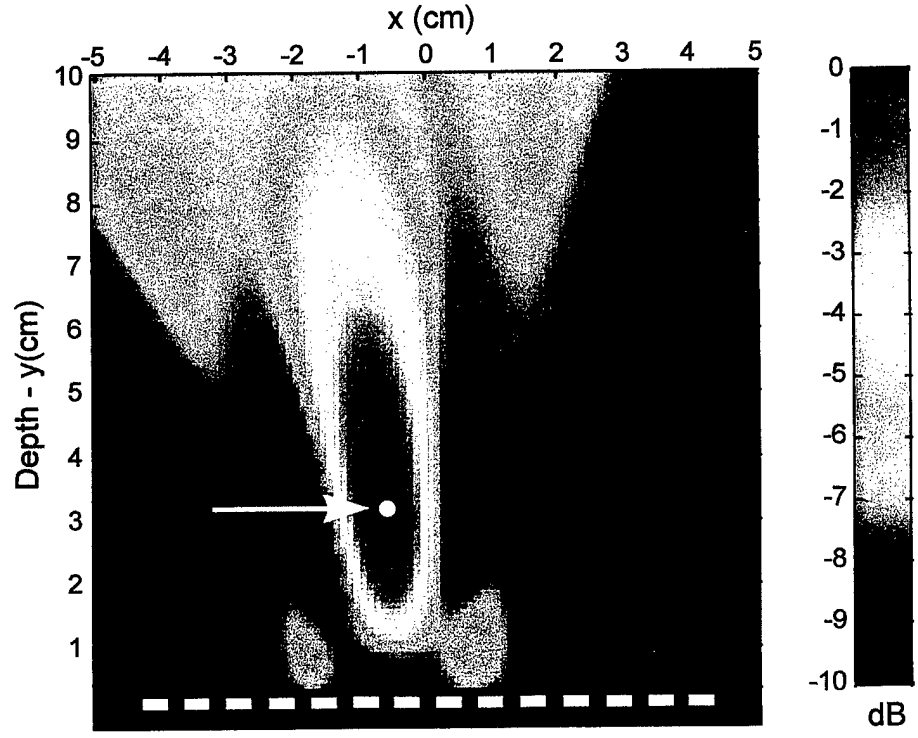

Figure 30. CFB for Simulation Two at 200 Hz

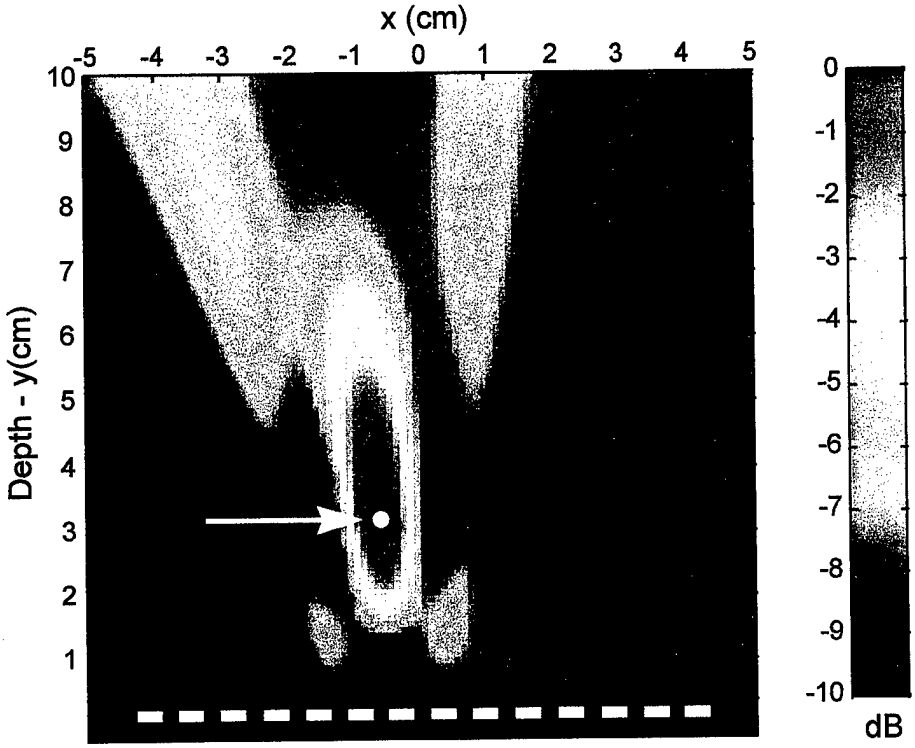

Figure 31. CFB for Simulation Two at 400 Hz

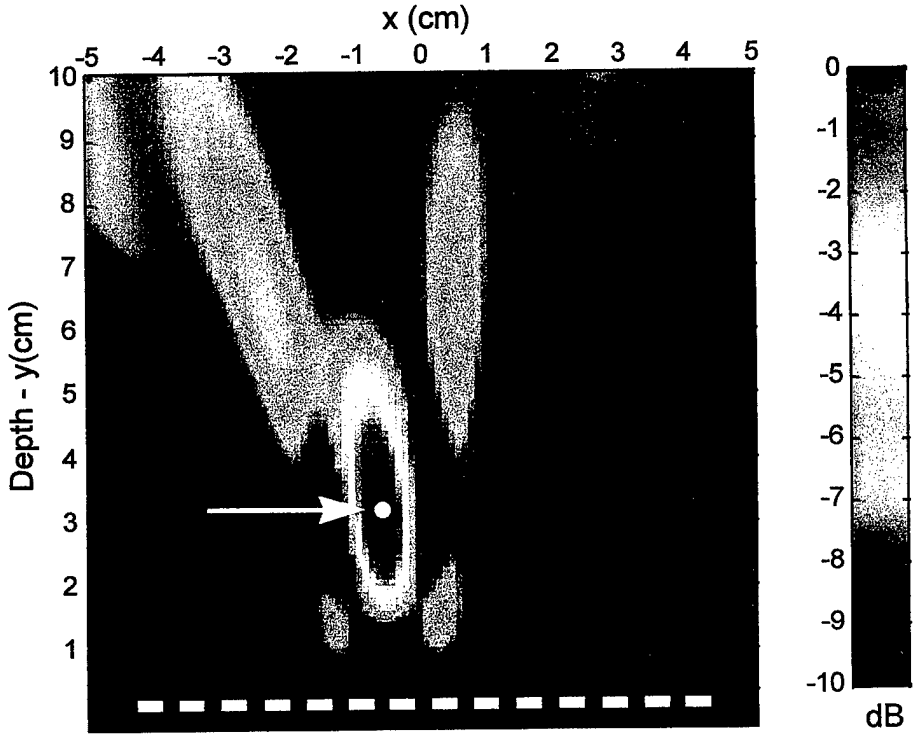

Figure 32. CFB for Simulation Two at 600 Hz

4.3. TWO CORRELATED PLANAR SOURCES

The third simulation is that of two correlated planar sources, one of which represents the heart wall and the other the interventricular septum. The energy in each planar source is correlated and corresponds to a membrane excited with an equal amount of energy at the same time across the entire surface. The model of the front planar source (heart wall) is 0.102 m (4 in.) long and 0.102 m (4 in.) high, and it is discretized with 289 spherical radiators, 17 of which are spaced 0.00635 m (0.250 in.) apart in both height and depth. This front source is parallel to the linear receiver (simulated array). The model of the back planar source (septum) is 0.0381 m (1.5 in.) long and 0.102 m (4 in.) high, and it is discretized using 102 spherical radiators, with 6 in the depth direction and 17 in the height direction, all of which are spaced 0.00635 m (0.250 in.) apart. This back source is orthogonal to the simulated array. The 0.250-in. spacing of the planar sources is considered sufficient to model the dynamics of the heart wall and septum because this is the spacing of the elements of the array and because all of the sources are coherent, which means that there are no spatial variations across either the heart wall or the septum. The geometry of this simulation is shown in figure 33.

All the radiators on each planar source transmit energy "in phase" and at the same power level, which means that the entries of each individual source CSDM are equal to equation (15). The final source CSDM is written as

$$\mathbf{E}(\omega_0) = \begin{bmatrix} \alpha_1 \mathbf{E_1}(\omega_0) & \mathbf{0} \\ \mathbf{0} & \alpha_2 \mathbf{E_2}(\omega_0) \end{bmatrix}, \tag{16}$$

where α_1 denotes the power of the first source and α_2 denotes the power of the second source. The power distribution between the sources is constrained by the equation

$$\alpha_1 + \alpha_2 = 1 . \tag{17}$$

Note that the coherence of each source is independent of the other source. Once the source CSDM is known, the steering vector $\mathbf{D}(\omega_0)$ is assembled using

$$\mathbf{D}(\omega_0) = \left[\mathbf{D_1}(\omega_0) \quad \mathbf{D_2}(\omega_0)\right], \tag{18}$$

and the simulated CSDM can be determined from equation (12). For this simulation, the power of the first source (α_1) was 0.909 and the power of the second source (α_2) was 0.0909. No power levels between the heart wall and the septum were found in the literature, so these numbers are a first rough estimate. Note that this does not constitute a total power ratio of 10:1 because the front source has 289 individual radiators and the back source has 102. The signal at the peak of the spatial spectrum (σ_s^2) was 1, and the power of the zero-mean, spatially uncorrelated additive noise at each sensor (σ_0^2) was 0.01.

Figures 34, 35, 36, and 37 are RVDR images of the simulation at 50, 200, 400, and 600 Hz, respectively, with the scalar enhancement factor (e) set to 0.01. The physical location of the planar sources is denoted with two black lines. The sources also have extent in the z-direction, which cannot be shown due to the two-dimensional properties of the image. Figures 38, 39, 40, and 41 are CFB images of the simulation at 50, 200, 400, and 600 Hz, respectively. The normalization factors of the images are listed in table 4.

The RVDR beamforming suppresses the coherent planar source (heart wall) that is parallel to the array and is incapable of entirely resolving the planar source (septum) that is orthogonal to the array. This suppression occurs even though the parallel planar source has 10 times as much power as the orthogonal planar source. Changing the power distribution between the two sources does not significantly affect any of the images. Furthermore, as the frequency increases, RVDR is losing its dynamic range. The end-effect energy that was present in the RVDR correlated linear source simulations is also present in the RVDR planar source simulations. The CFB is incapable of resolving either planar source.

Table 4. Image Normalization Factors in Decibels for the Third Simulation

Frequency (Hz)	RVDR	CFB
50.0	-12.8	10.6
200.0	-14.0	8.3
400.0	-16.9	5.8
600.0	-15.0	5.5

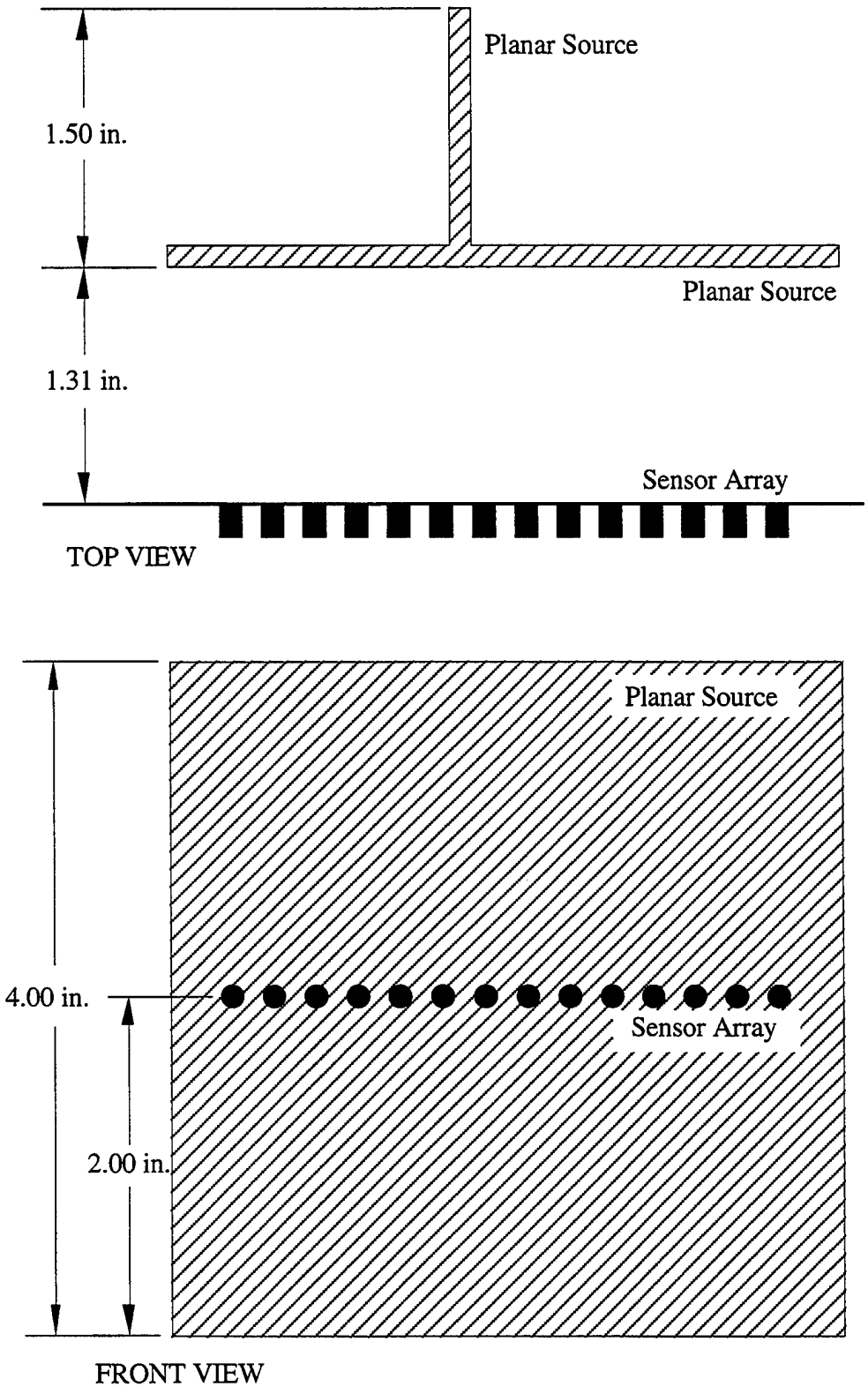

Figure 33. Geometry of the Simulations with Planar Sources

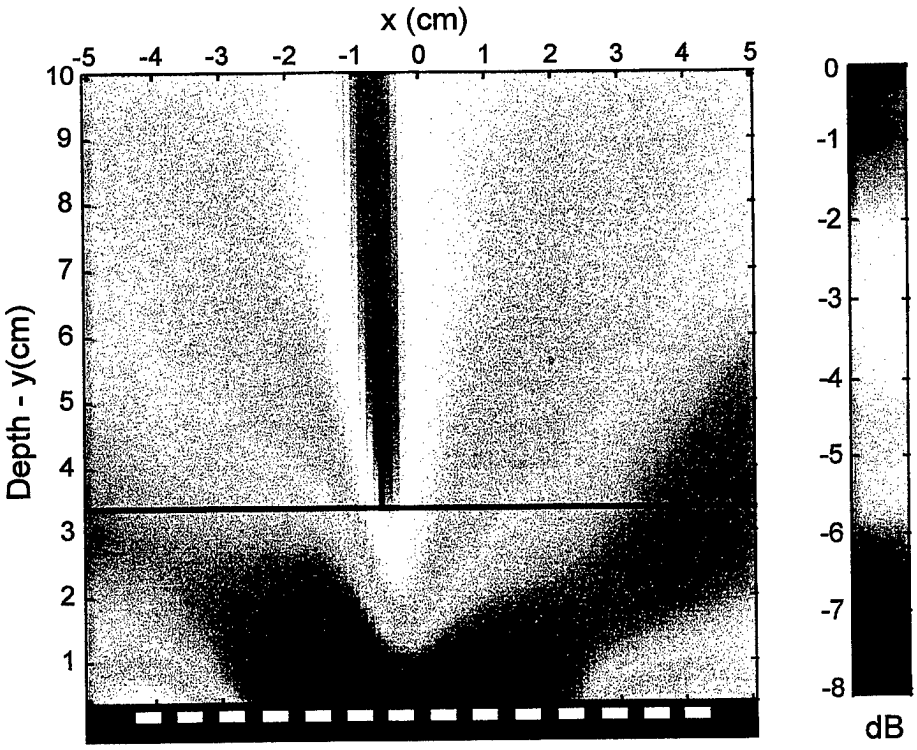

Figure 34. RVDR for Simulation Three at 50 Hz

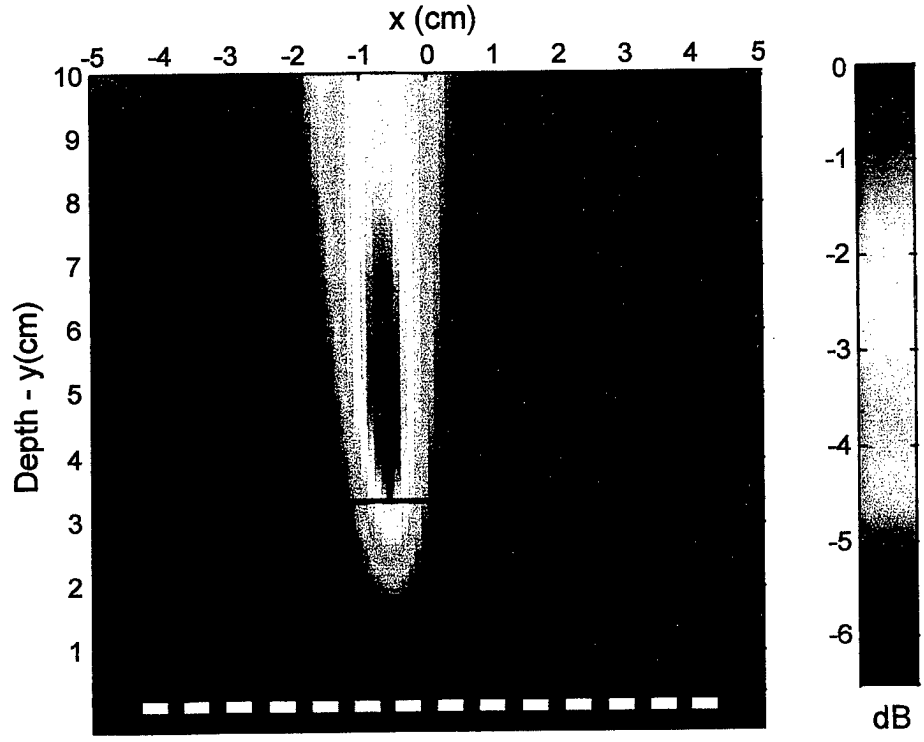

Figure 35. RVDR for Simulation Three at 200 Hz

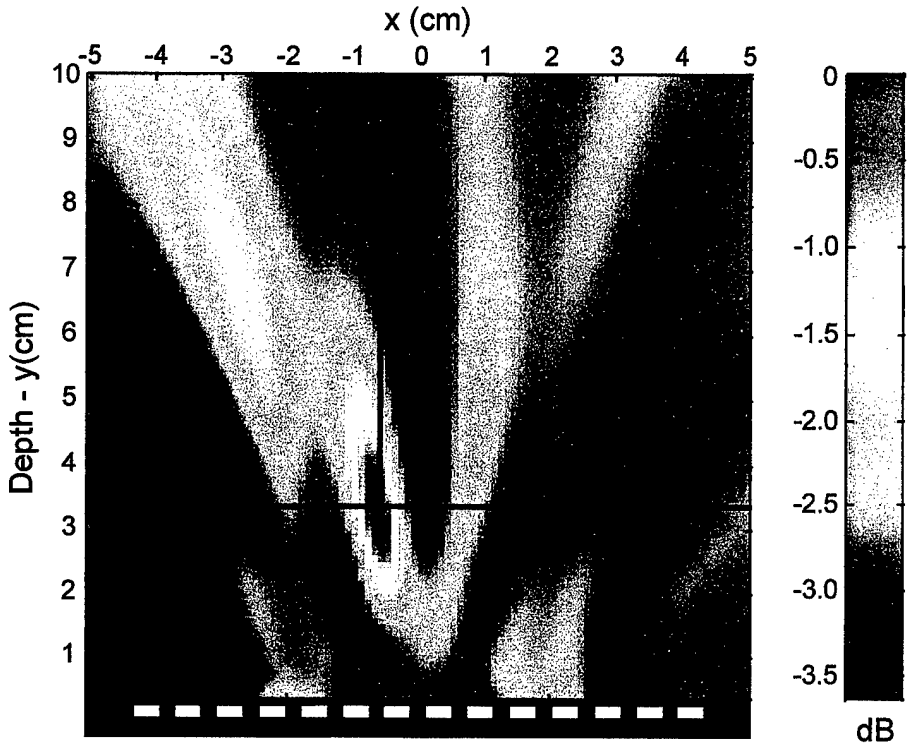

Figure 36. RVDR for Simulation Three at 400 Hz

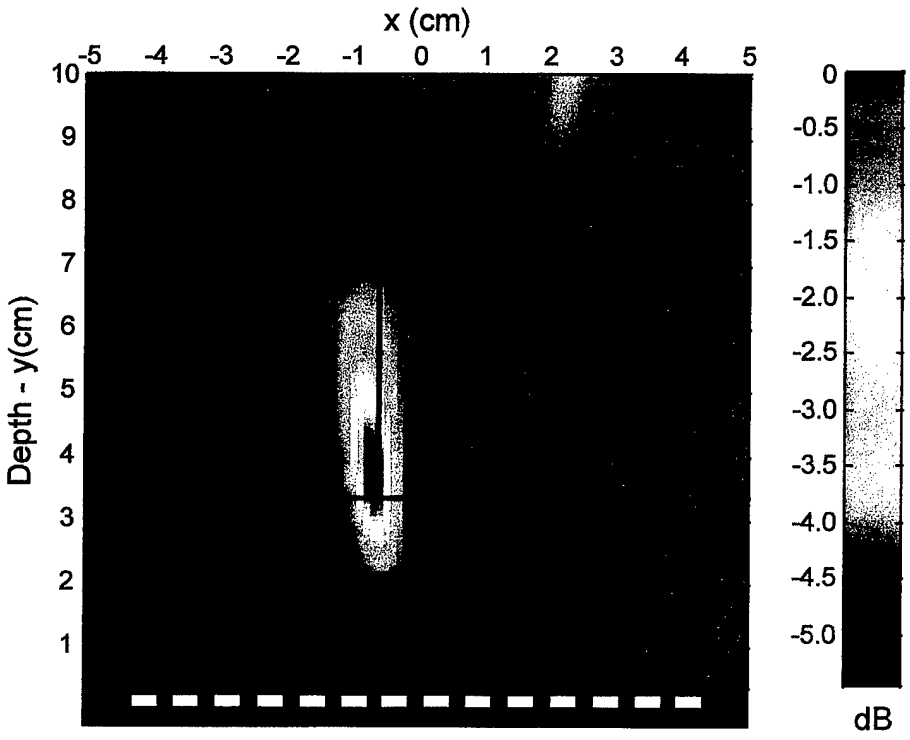

Figure 37. RVDR for Simulation Three at 600 Hz

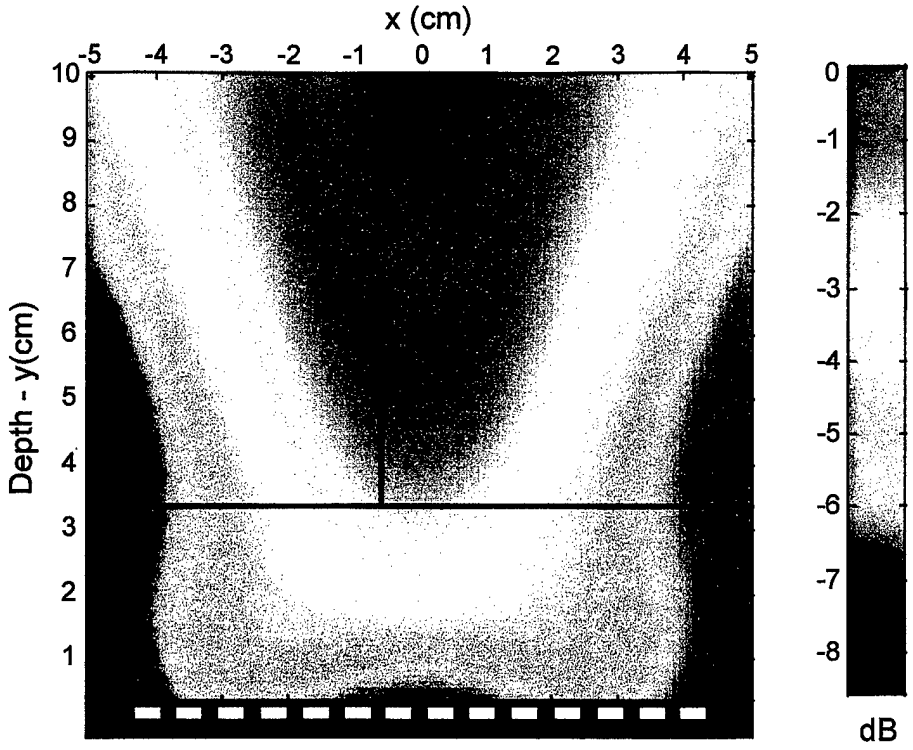

Figure 38. CFB for Simulation Three at 50 Hz

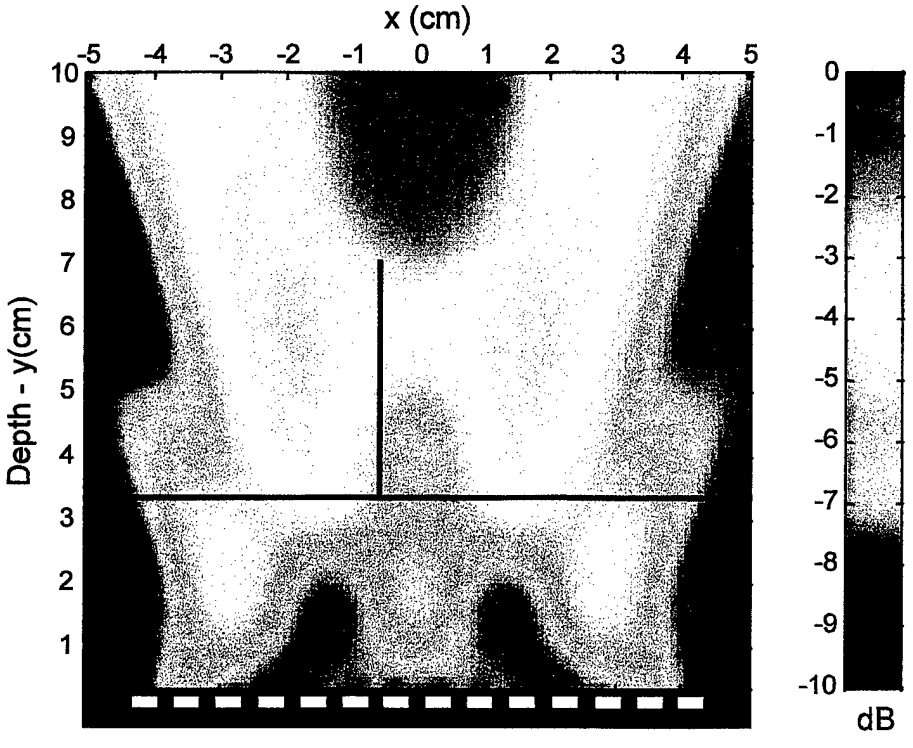

Figure 39. CFB for Simulation Three at 200 Hz

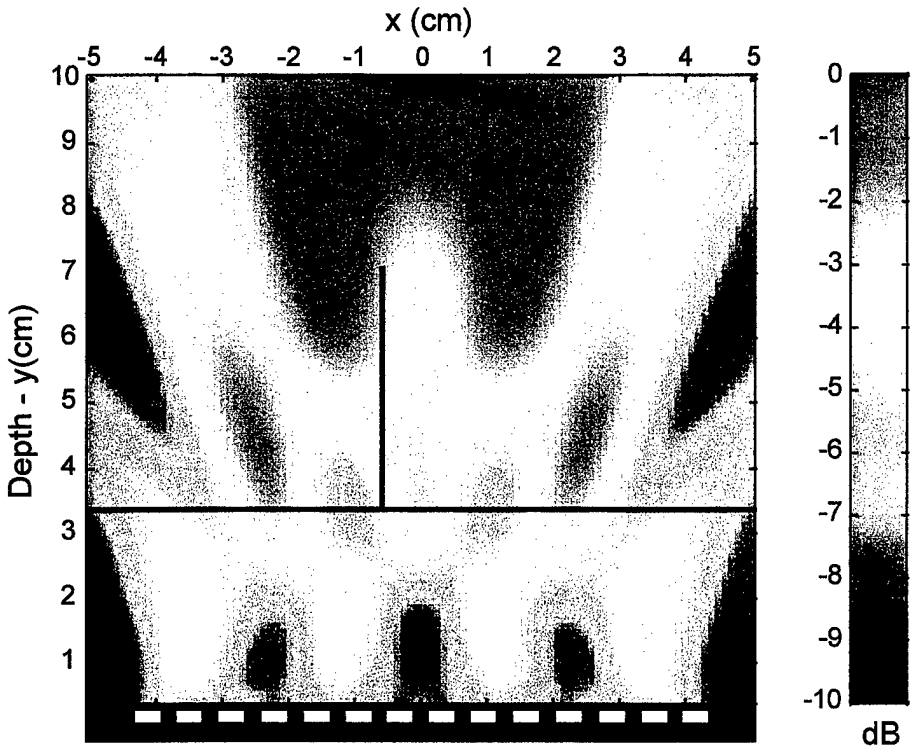

Figure 40. CFB for Simulation Three at 400 Hz

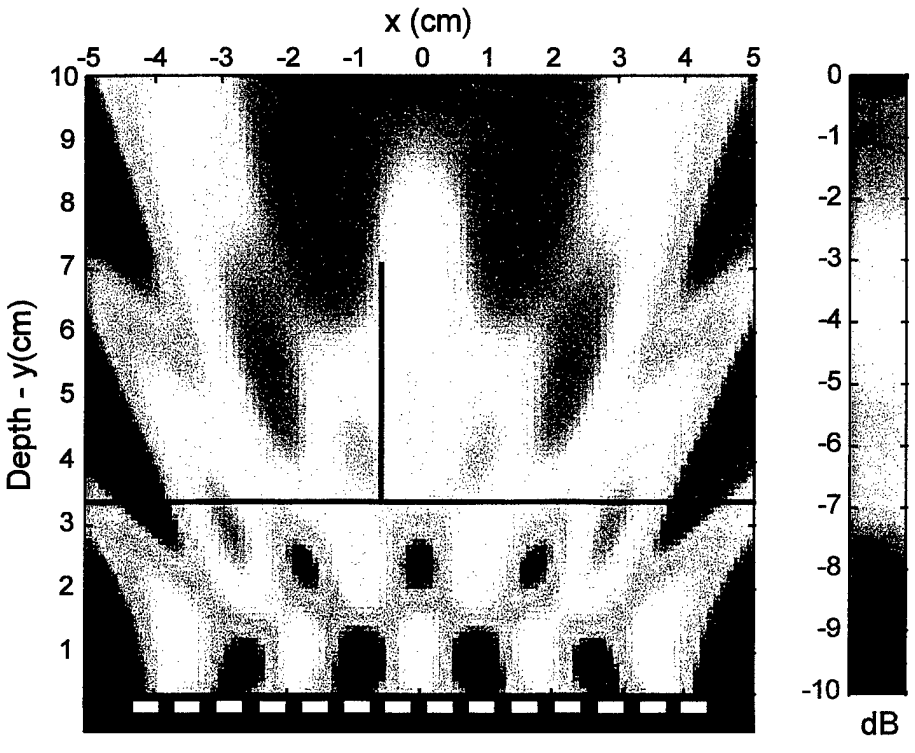

Figure 41. CFB for Simulation Three at 600 Hz

4.4. A SINGLE NEARLY UNCORRELATED LINE SOURCE WITH TWO CORRELATED PLANAR SOURCES

The fourth simulation is a geometrical combination of the first and third simulation. It consists of a linear source, a front planar source, and a rear planar source that represent the LAD artery, heart wall, and septum, respectively. The geometry of this simulation is shown in figure 42. Source one is the linear source and equation (11) is used to form the source CSDM. Source two is the front planar source and source three is the back planar source; equation (15) is used to form each planar source CSDM. Once each source CSDM is defined, they are assembled into a single source CSDM with

$$\mathbf{E}(\omega_0) = \begin{bmatrix} \alpha_1\mathbf{E_1}(\omega_0) & \mathbf{0} & \mathbf{0} \\ \mathbf{0} & \alpha_2\mathbf{E_2}(\omega_0) & \mathbf{0} \\ \mathbf{0} & \mathbf{0} & \alpha_3\mathbf{E_3}(\omega_0) \end{bmatrix}, \tag{19}$$

where α denotes the power distribution between the sources, which is constrained by the equation

$$\alpha_1 + \alpha_2 + \alpha_3 = 1\,. \tag{20}$$

Note that the three sources have no intersource coherence because there are zeros in the off-diagonal blocks in the source coherence matrix of equation (19). Once the source CSDM is known, the steering vector $\mathbf{D}(\omega_0)$ is assembled from

$$\mathbf{D}(\omega_0) = \left[\mathbf{D_1}(\omega_0) \quad \mathbf{D_2}(\omega_0) \quad \mathbf{D_3}(\omega_0)\right], \tag{21}$$

and the simulated CSDM can be determined from equation (12).

This simulation was analyzed with two different source power levels: one has the LAD artery with a small power level and one has the LAD artery with a large power level. The first, denoted case one, used a power distribution of α_1 = 0.0833, α_2 = 0.833, and α_3 = 0.0833. The second, denoted case two, used a power distribution of α_1 = 0.694, α_2 = 0.278, and α_3 = 0.0278. The signal at the peak of the spatial spectrum (σ_s^2) was 1, and the power of the zero-mean, spatially uncorrelated additive noise at each sensor (σ_0^2) was 0.01.

Figures 43, 44, 45, and 46 are RVDR images of the simulation for case one at 50, 200, 400, and 600 Hz, respectively, with the scalar enhancement factor (e) set to 0.01. Figures 47, 48, 49, and 50 are RVDR images of the simulation for case two at 50, 200, 400, and 600 Hz, respectively, with the scalar enhancement factor (e) set to 0.01. The normalization factors of the images are listed in table 5.

The physical location of the planar sources is denoted with two black lines and the linear source with a black circle. Note that as the power in the linear source (LAD artery) increases, it is resolvable from the planar sources (septum and anterior heart wall). Additionally, the amount of energy imaged behind the septum is increasing as the LAD energy level increases.

Most notable from all the images is that the RVDR beamformer cannot observe the heart wall regardless of how much energy it possesses. This occurs because the RVDR focused beamformer assumes an incoherent single source model for the beam formation algorithm derivation. This assumption is invalid for the extended sources, which represent both the anterior heart wall and the septum. The consequence of this beamformer source model mismatch is a suppression of the actual source energy that has not been properly represented by the model. In the case of the anterior heart wall, numerical simulations suggest that the distributed coherent source results in the complete suppression of the wall energy from the image. Because the fundamental resolution of the focused beamformer in depth (y-axis) is less than in the anterior wall (x-axis) dimension and because the source level is lower, the simulated septum extended source is not completely suppressed. The CFB images for this simulation are not shown, but they are very similar to figures 38-41.

Table 5. Image Normalization Factors in Decibels for the Fourth Simulation

Frequency (Hz)	Case One	Case Two
50.0	-12.7	-13.5
200.0	-12.8	-13.9
400.0	-13.2	-14.0
600.0	-12.1	-11.5

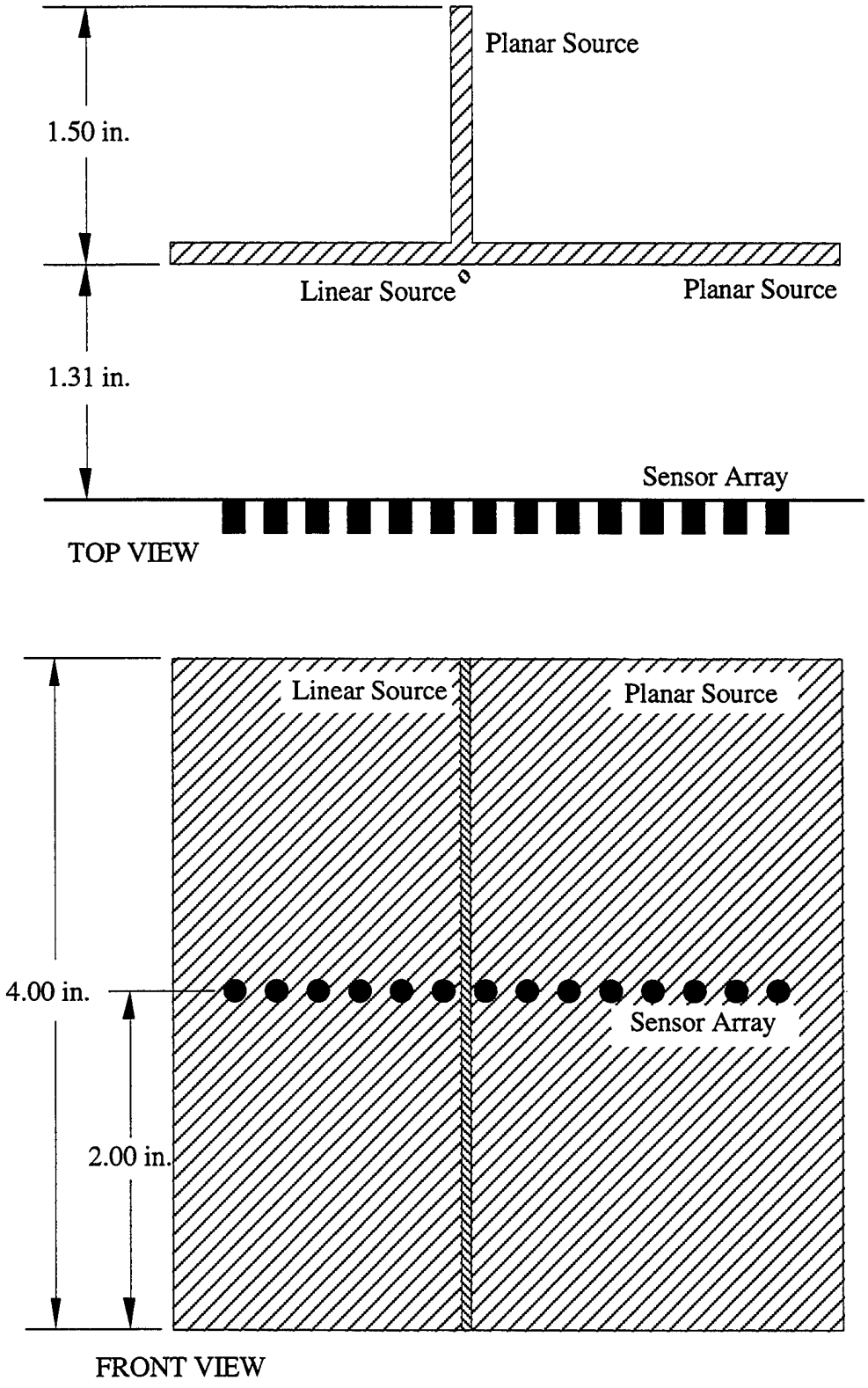

Figure 42. Geometry of the Simulations with Linear and Planar Sources

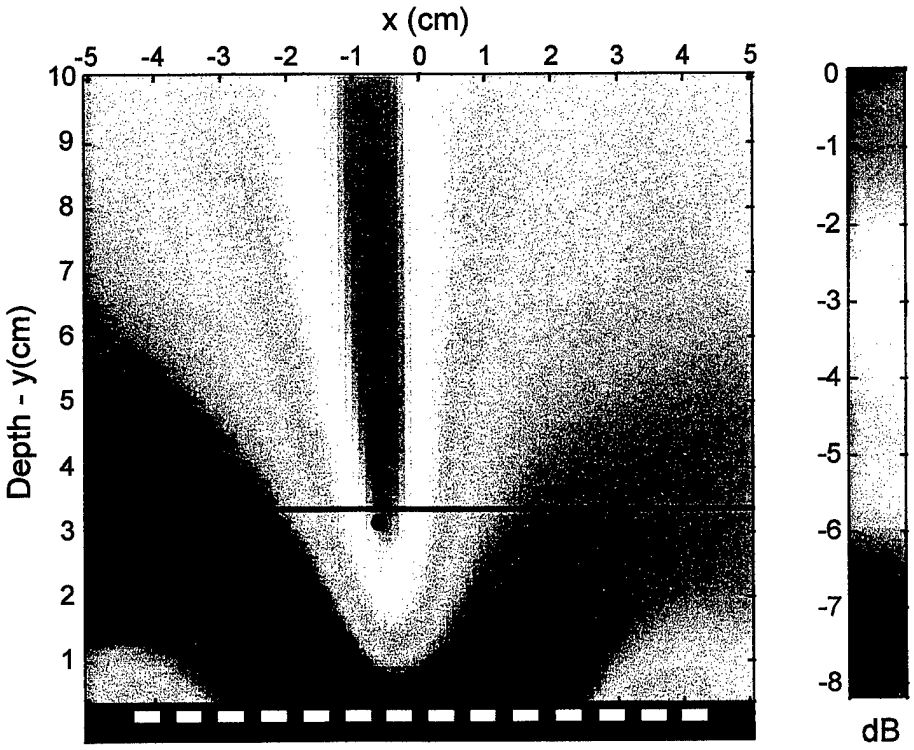

Figure 43. RVDR for Simulation Four (Case One) at 50 Hz

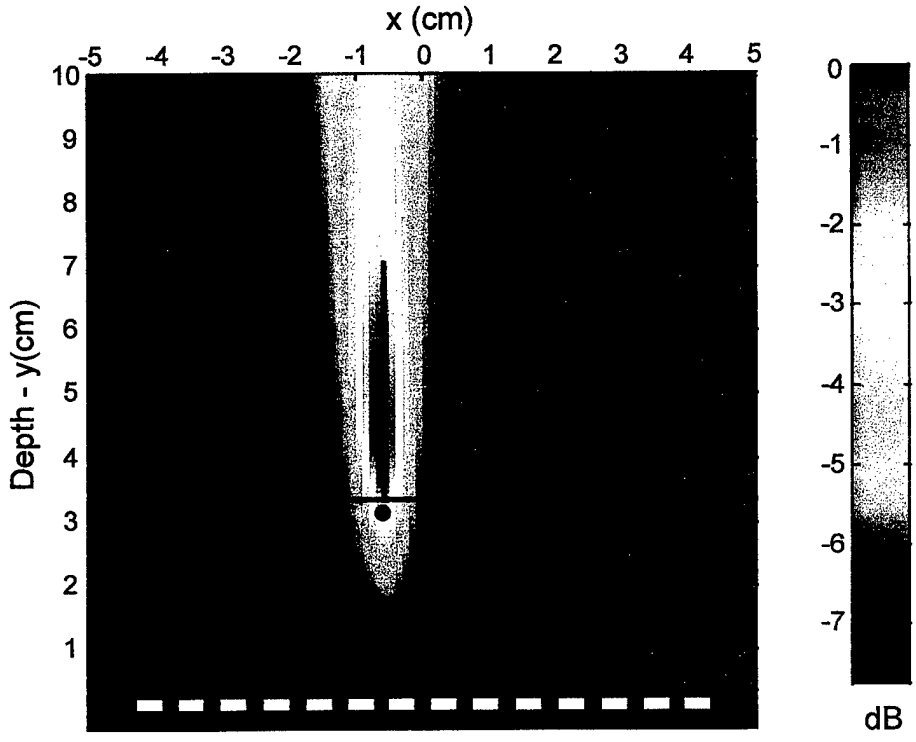

Figure 44. RVDR for Simulation Four (Case One) at 200 Hz

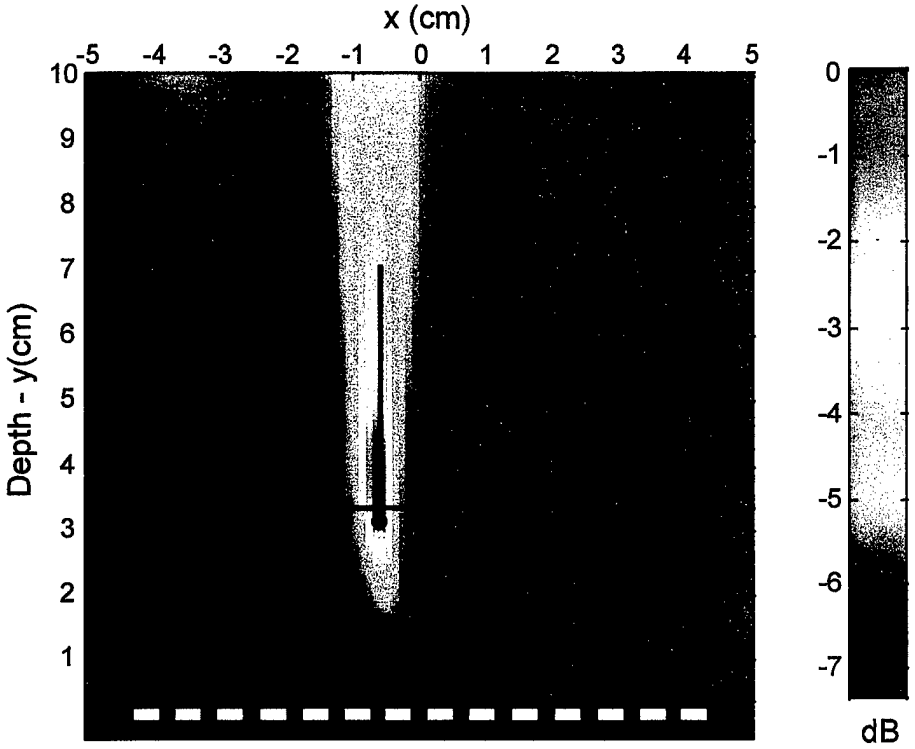

Figure 45. RVDR for Simulation Four (Case One) at 400 Hz

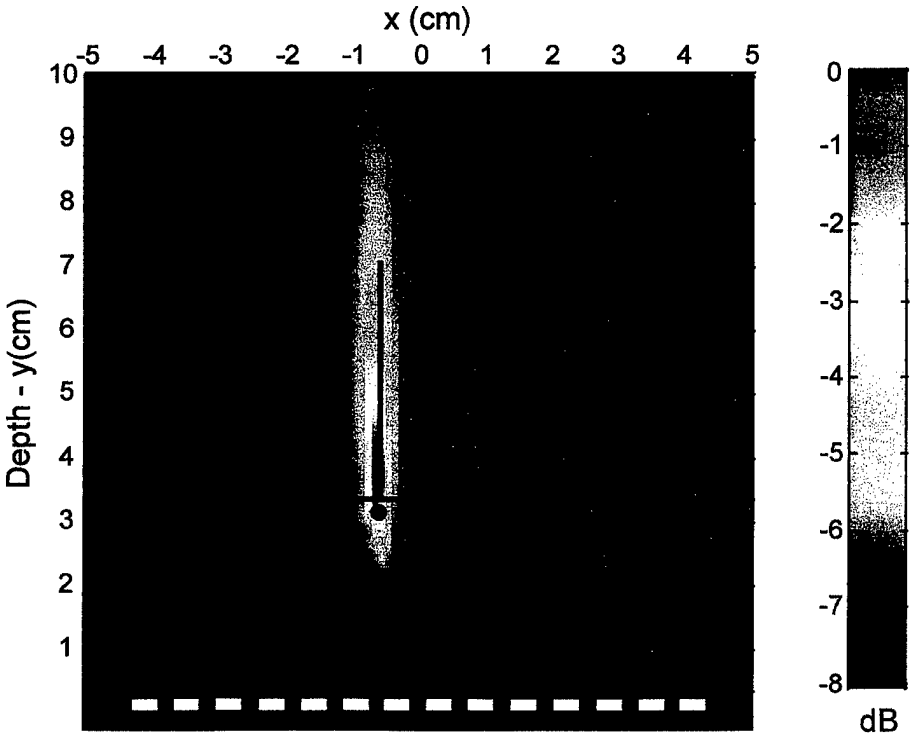

Figure 46. RVDR for Simulation Four (Case One) at 600 Hz

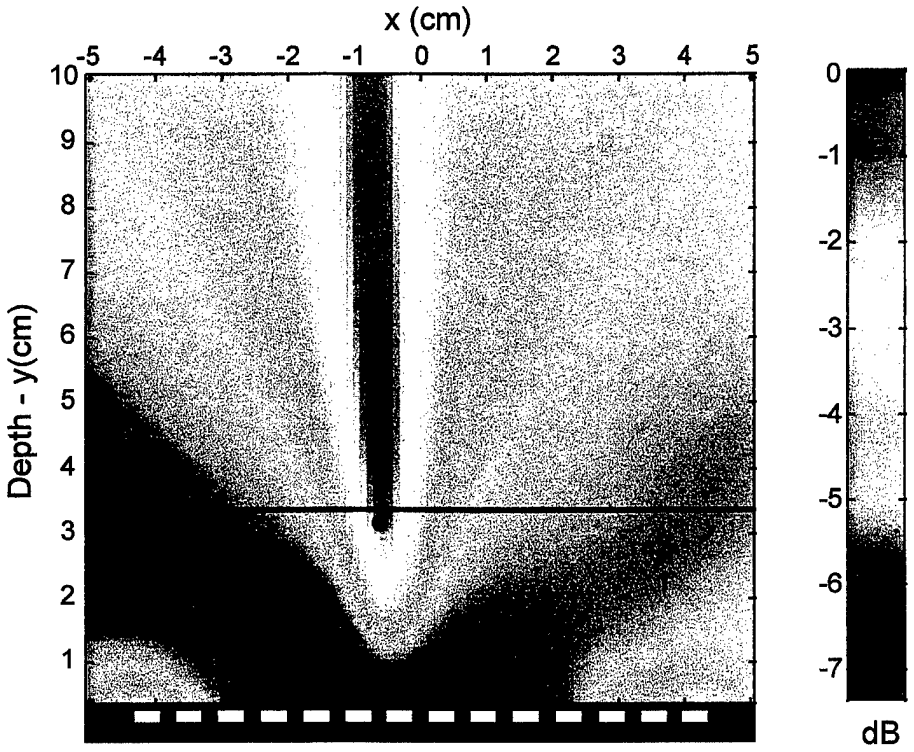

Figure 47. RVDR for Simulation Four (Case Two) at 50 Hz

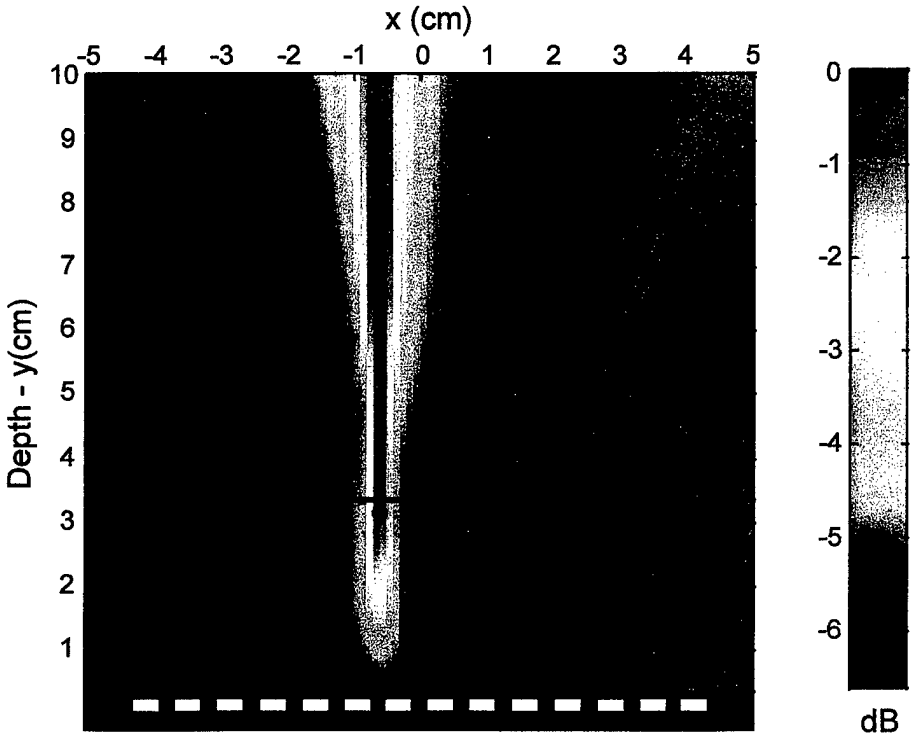

Figure 48. RVDR for Simulation Four (Case Two) at 200 Hz

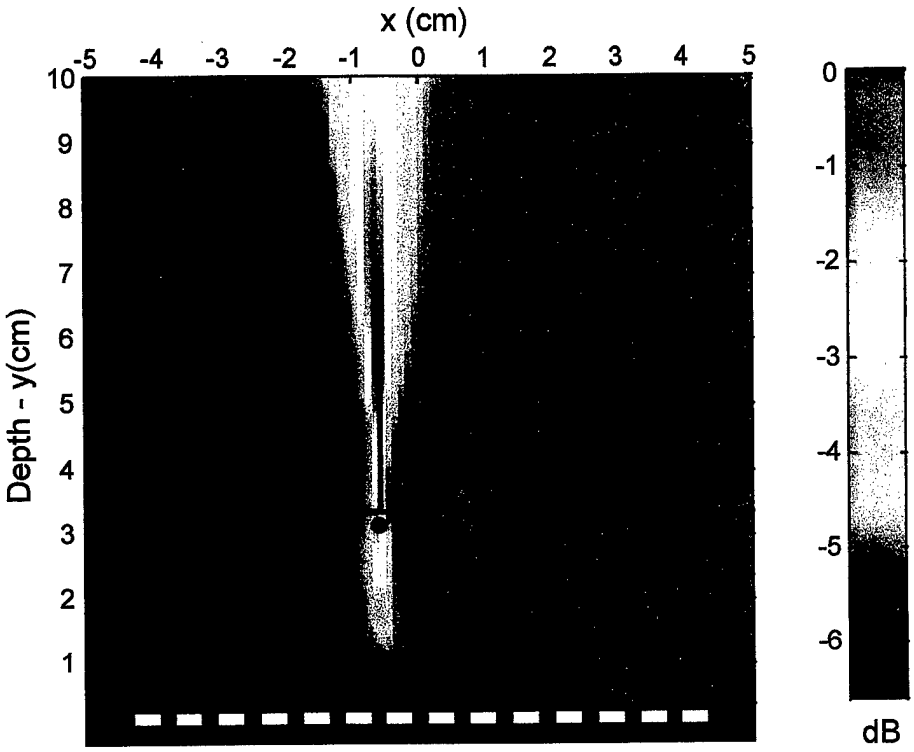

Figure 49. RVDR for Simulation Four (Case Two) at 400 Hz

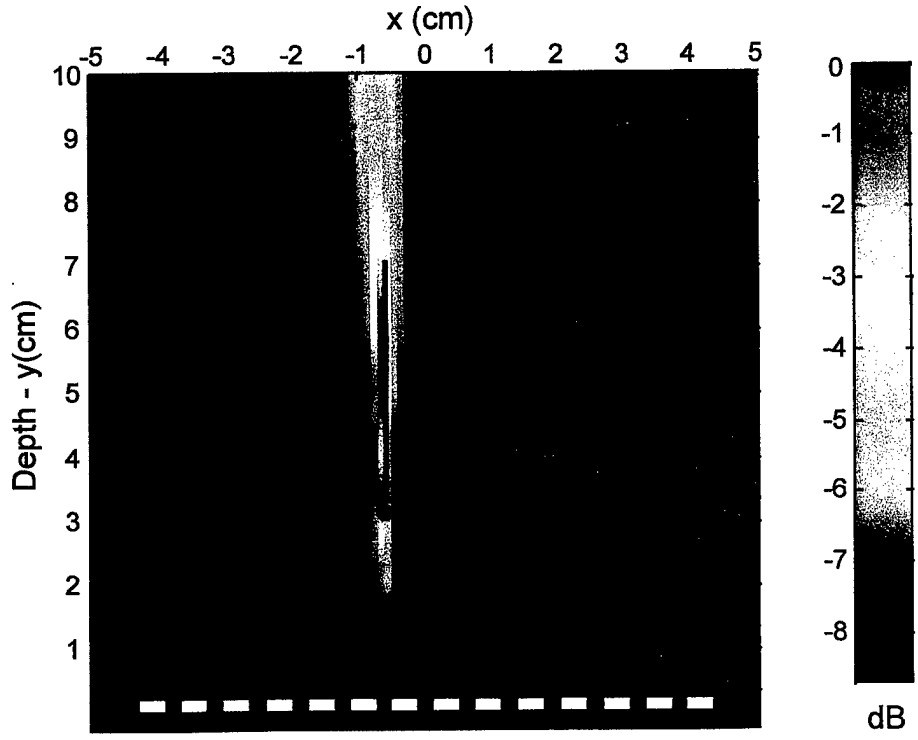

Figure 50. RVDR for Simulation Four (Case Two) at 600 Hz

4.5. A SINGLE CORRELATED LINE SOURCE WITH TWO CORRELATED PLANAR SOURCES

The fifth simulation is the same as the fourth simulation, except that the linear source is totally correlated. The geometry of this simulation is shown in figure 42. Source one is the linear source (LAD artery) and equation (15) is used to form the source CSDM. Source two is the front planar (anterior) heart-wall-simulated source, and source three is the back planar septum-simulated source; equation (15) is used to form each planar source CSDM. This simulation was conducted with two cases, each having a different source power level: case one has the linear source (LAD artery) with a low power level and case two has the linear source (LAD artery) with a high power level relative to the level of the anterior heart-wall-simulated source. Case one used a power distribution of $\alpha_1 = 0.0833$, $\alpha_2 = 0.833$, and $\alpha_3 = 0.0833$. Case two used a power distribution of $\alpha_1 = 0.694$, $\alpha_2 = 0.278$, and $\alpha_3 = 0.0278$. The signal at the peak of the spatial spectrum (σ_s^2) was 1, and the power of the zero-mean, spatially uncorrelated additive noise at each sensor (σ_0^2) was 0.01.

Figures 51, 52, 53, and 54 are RVDR images of the simulation for case one at 50, 200, 400, and 600 Hz, respectively, with the scalar enhancement factor (e) set to 0.01. Figures 55, 56, 57, and 58 are RVDR images of the simulation for case two at 50, 200, 400, and 600 Hz, respectively, with the scalar enhancement factor (e) set to 0.01. The normalization factors of the images are listed in table 6.

The images for both cases are similar, although the figures in case two have less dynamic range, indicating that there is more source energy suppression. In this example, as well as in the fourth simulation, detection of the linear source simulating the LAD artery results in a signal level (in the LAD) versus background signal level (in the septum) problem. However, the energy from the front planar source (anterior heart wall), which is being dramatically suppressed, does not affect the image. The CFB images for this simulation are not shown, but for case one they are very similar to figures 38-41 and for case two they are very similar to figures 29-32.

The important technical issue here concerns quantifying the exact level of valve flow-induced energy propagating in the atrial-ventricular anterior heart wall and septum relative to LAD artery energy.

Table 6. Image Normalization Factors in Decibels for the Fifth Simulation

Frequency (Hz)	Case One	Case Two
50.0	-13.3	-16.5
200.0	-13.7	-16.9
400.0	-17.6	-19.0
600.0	-16.6	-19.1

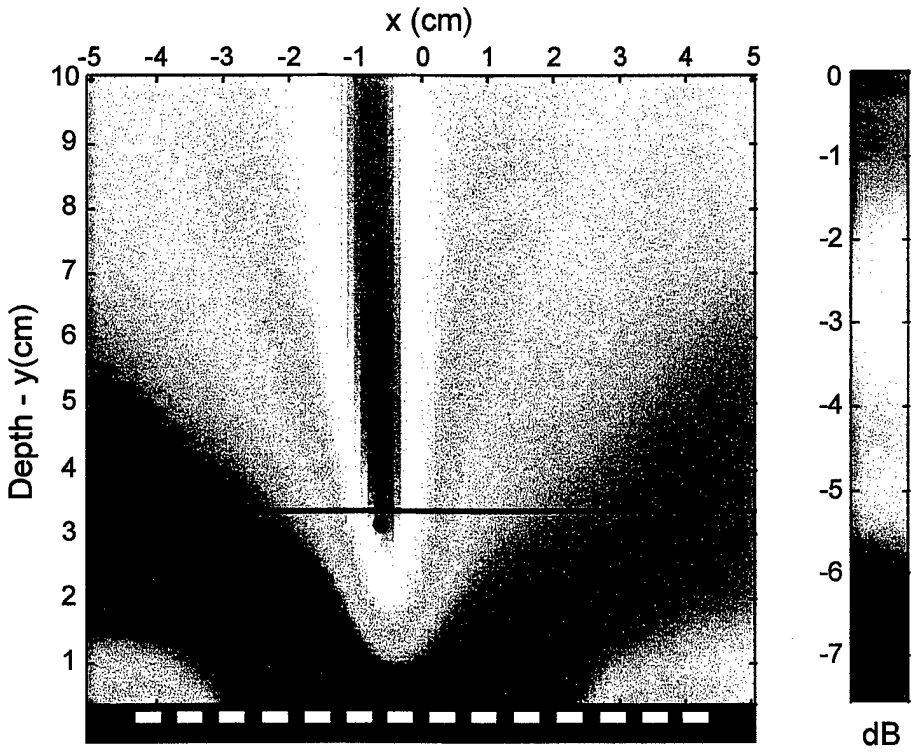

Figure 51. RVDR for Simulation Five (Case One) at 50 Hz

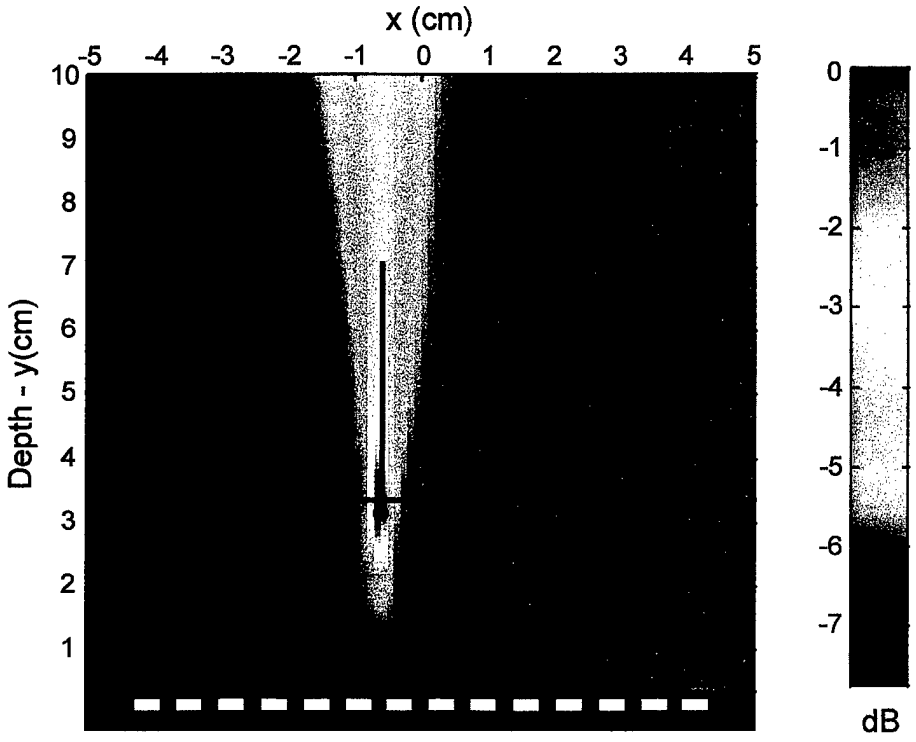

Figure 52. RVDR for Simulation Five (Case One) at 200 Hz

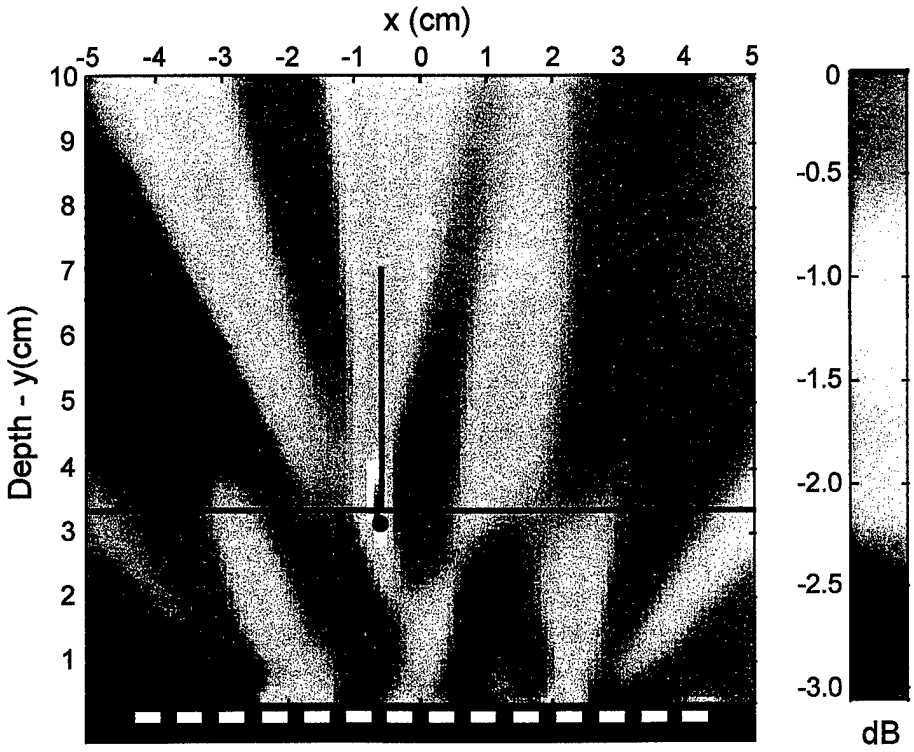

Figure 53. RVDR for Simulation Five (Case One) at 400 Hz

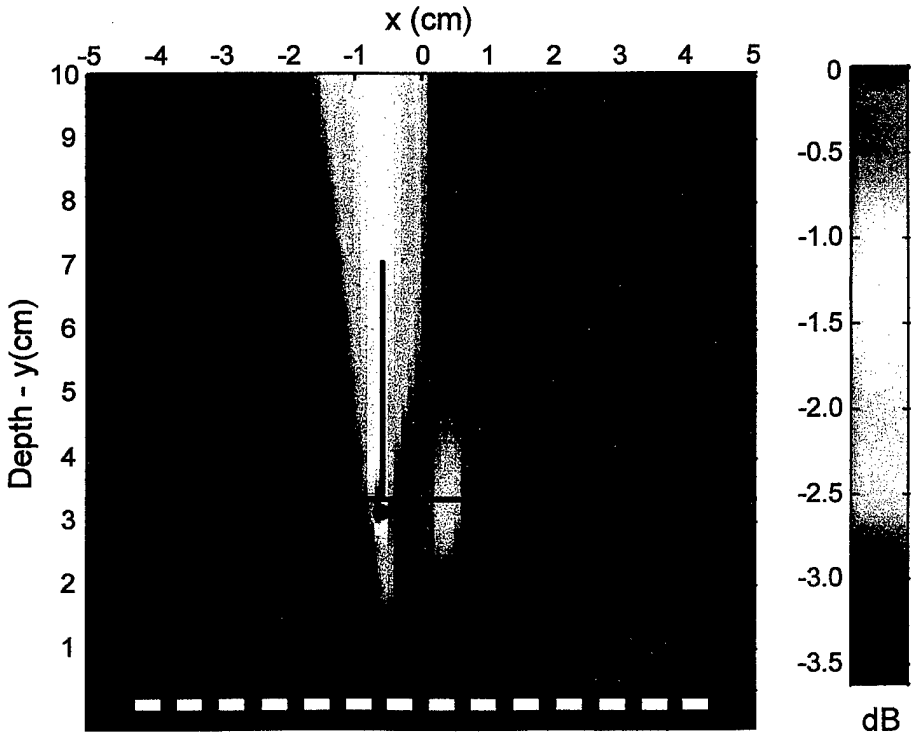

Figure 54. RVDR for Simulation Five (Case One) at 600 Hz

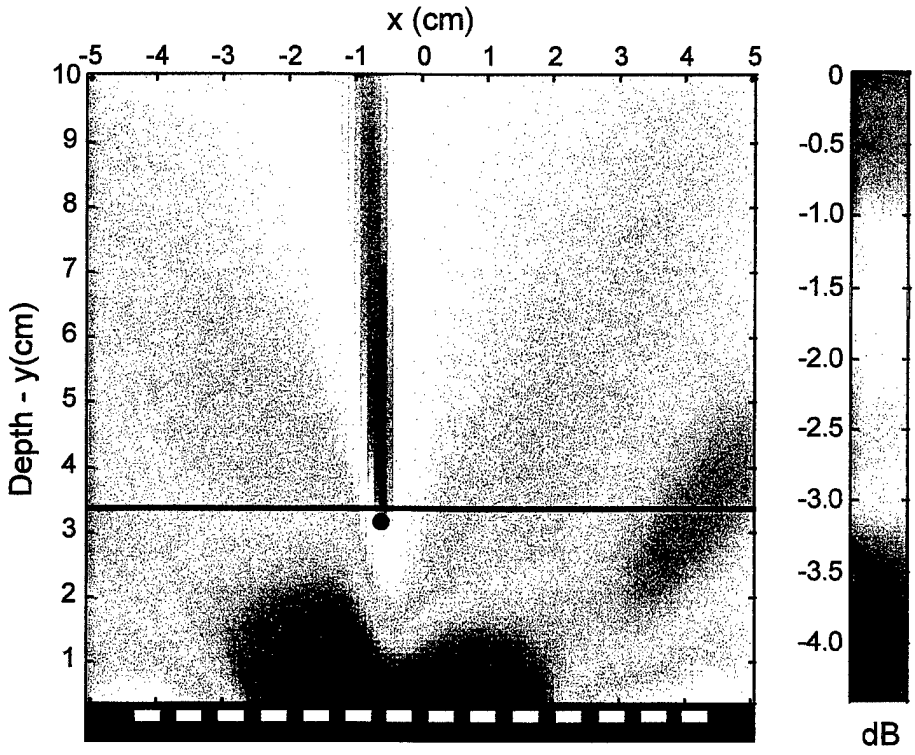

Figure 55. RVDR for Simulation Five (Case Two) at 50 Hz

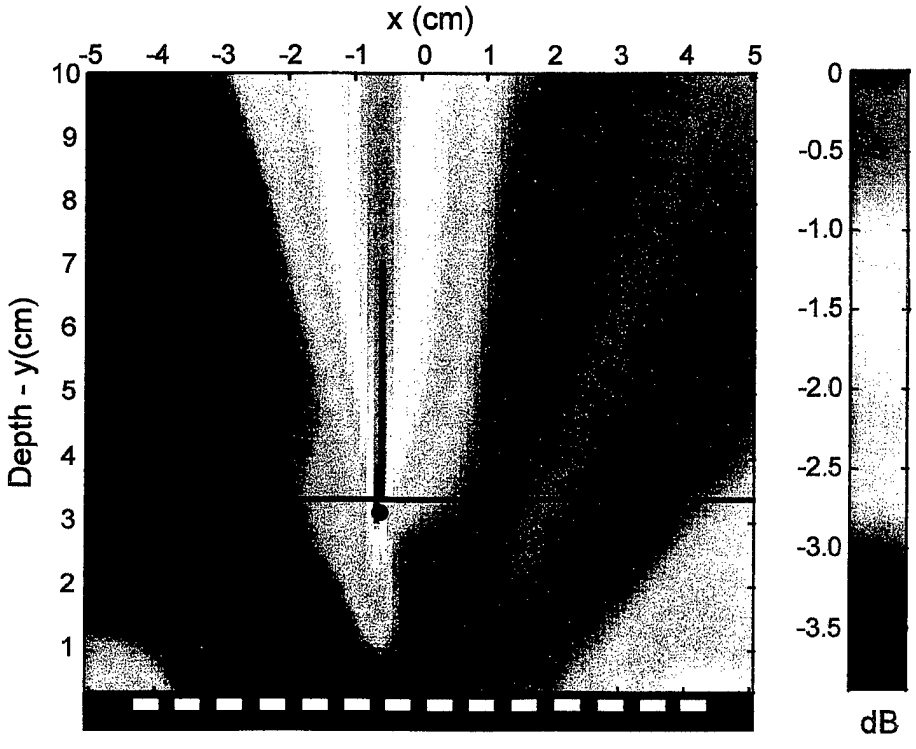

Figure 56. RVDR for Simulation Five (Case Two) at 200 Hz

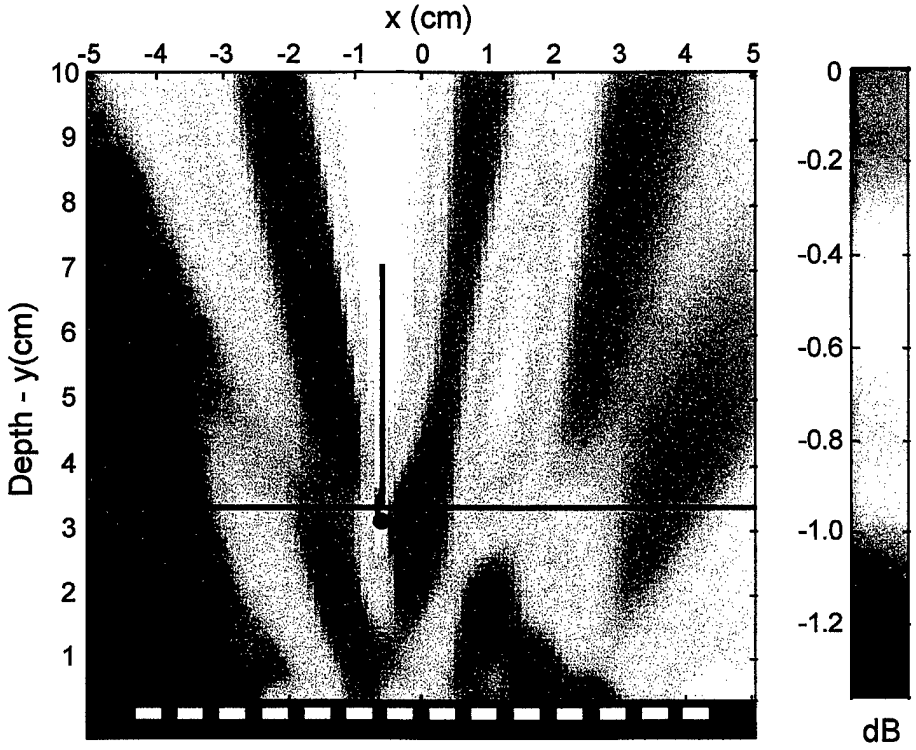

Figure 57. RVDR for Simulation Five (Case Two) at 400 Hz

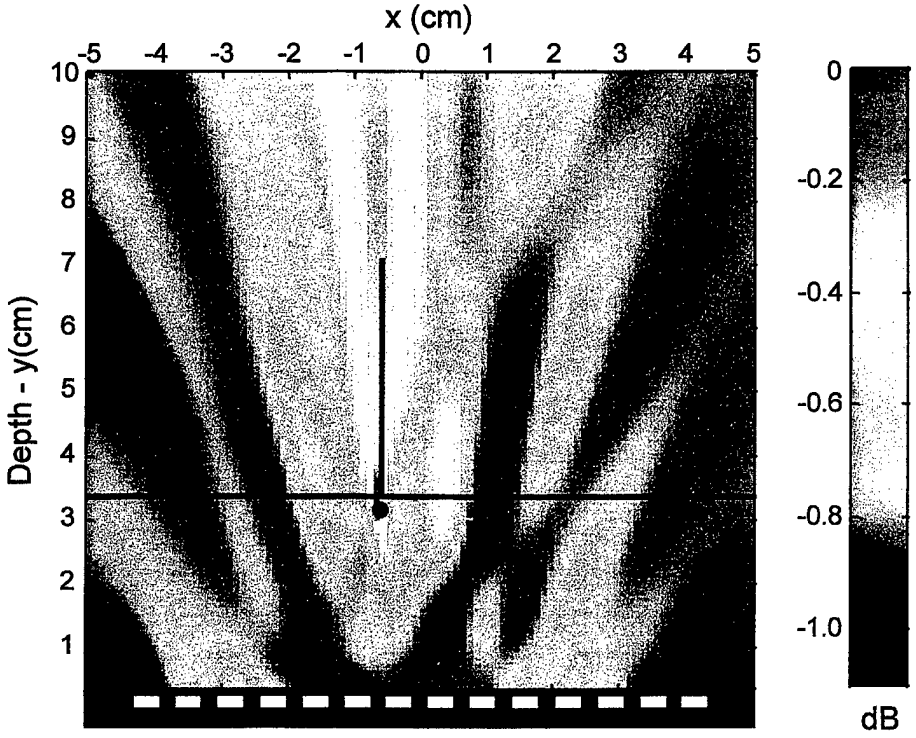

Figure 58. RVDR for Simulation Five (Case Two) at 600 Hz

5. DISCUSSION

The simulations that provide RVDR beamformer images most similar to human data images are simulations four and five. Specifically, figures 3 through 8 correspond very closely to figures 43-58, with one major exception: the simulation is starting to locate the source in depth where the actual human data does not provide any depth localization.

There are several reasons why this may be occurring. First, the patient had a triple branch point (trifurcation) in the LM coronary artery, which is located upstream of the LAD artery. Noise mechanisms at this location may be entering the beam of the array, especially when the array beam is steered into the chest at locations near a depth of 10 cm. Due to the geometrical configuration of the array, the beam admits energy from an annulus of locations at a constant radial distance rather than just the desired focal point. The upstream energy from this trifurcation is not present in the simulation, and thus the localization (in the simulation) of the source is more concise. Another reason is that the parametric mismatch in the RVDR beamformer during the human experiment may be significant, which is causing a "focusing extension" behind the LAD. High-resolution beamformers, such as RVDR, are sensitive to mismatch in such parameters as exact sensor location. A third reason is that there may actually be an energy source behind the septum and the LAD in the heart region. It is possible that this other energy is being measured by the array during the diastolic phase of the heart cycle. Fourth, the simulation uses a relatively simple model of the geometry. This model assumes that the medium is homogeneous and supports shear wave energy at every location. This inaccurate approximation of the human thorax, which, in reality, contains ribs that scatter and reradiate energy and fluids that do not support shear wave mechanisms, can cause a difference between the model and the measurements.

The CFB images from the human data are very similar to the CFB images from simulation three, four (not shown), and five (not shown), although the beamformer does not localize the line source in any of the images. Figures 9-14 correspond very closely to figures 38-41, where the majority of the energy is located near the maximum value of depth in the images. The amount of normalization between the CFB and the RVDR beamformers, which is roughly equivalent for simulation four and the human data, indicates that both beamformers have approximately the same degree of model mismatch for propagating energy.

The apparent source of turbulent flow-related energy in the LAD artery is still an open issue. Blood is typically considered to have laminar flow in healthy arteries,[7] although turbulent flow is possible near arterial branch points (bifurcations and trifurcations).

Additionally, turbulent flow is frequently present downstream of a stenosis[8] and sometimes a newly implanted stent. Wave motion in the artery wall is also a possible source because different types of waves can propagate up and down the artery, transmitting energy into the surrounding soft tissue. These waves can be excited in a number of ways: turbulence in the artery, motion at the start or near the end of the artery, or even motion from the coupling of a fluid and a solid.[9] Resolution of the wall motion issue will enhance the understanding of the beamformed images.

6. CONCLUSIONS AND RECOMMENDATIONS

Vibrational energy propagating in the LAD coronary artery, the anterior heart wall, and the interventricular septum in a human has been modeled and imaged using an RVDR beamformer. The simulations show that passive imaging of the LAD artery is possible if there is enough energy in the LAD relative to the heart wall and the septum. The septum was localized in the dimension across the human chest, but the depth localization is ambiguous because of the rotational properties of the linear array used in both the human measurements and the simulations.

Simulations that model the heart wall and septum as planar sources produce images that are similar to the human data. They specifically show that a low-level spatially coherent planar source (such as the septum) can be either imaged and localized or suppressed when oriented in a parallel plane relative to the receiving array. The effects of source coherence and spatial extent are included in the models, with similar effects noted in the experimental data.

Continuation of work in this area should include an emphasis on (1) depth localization, (2) signal processing techniques to separate the LAD artery and the septum vibrational fields, and (3) testing on humans with occluded LAD arteries.

The key structural acoustics issue that must be resolved in future work is the characterization of the valvular flow-induced energy that is propagating from the interchamber walls of the heart to the outer wall. This energy path may manifest itself as concentrated strips of energy on the anterior heart wall, which may not be spatially resolvable from vibrations due to blood flow turbulence in the coronary arteries.

7. REFERENCES

1. N. L. Owsley, A. J. Hull, M. H. Ahmed, and J. Kassal, "A Proof-of-Concept Experiment for the Detection of Occluded Coronary Arteries Using Array Sensor Technology," *1995 IEEE Engineering in Medicine & Biology 17th Annual Conference*, Montreal, Canada, September 1995.

2. S. Haykin, J. N. Justice, N. L. Owsley, J. L. Yen, and A. C. Kak, *Array Signal Processing*, Prentice-Hall, Inc., Englewood Cliffs, NJ, 1985.

3. A. J. Hull and N. L. Owsley, "Beamformed Nearfield Imaging of a Simulated Coronary Artery Containing a Stenosis," NUWC-NPT Technical Report 10,820, Naval Undersea Warfare Center Division, Newport, RI, 1997.

4. J. Verburg, "Transmission of Vibrations of the Heart to the Chestwall," *Advanced Cardiovascular Physiology*, Karger, Basel, vol. 5 (part III), 1983, pp. 84-103.

5. W. L. Keith and B. M. Abraham, "Effects of Convection and Decay of Turbulence on the Wall Pressure Wavenumber-Frequency Spectrum," *Journal of Fluids Engineering*, vol. 119, 1997, pp. 50-55.

6. C. A. Norton, "A Compilation of Geometric Distance and Tissue Property Data for the Human Thorax," NUWC-NPT Technical Document 11,037, Naval Undersea Warfare Center Division, Newport, RI, 1995.

7. D. F. Young, "Fluid Mechanics of Arterial Stenoses," *Journal of Biomechanical Engineering*, vol. 101, 1979, pp. 157-175.

8. R. J. Tobin and I. Chang, "Wall Pressure Spectra Scaling Downstream of Stenosis in Steady Tube Flow," *Journal of Biomechanics*, vol. 9, 1976, pp. 633-640.

9. H. Lamb, "On the Velocity of Sound in a Tube, as Affected by the Elasticity of the Walls," *Manchester Literary and Philosophical Society, Memoirs and Proceedings*, vol. 42(9), 1898, pp. 1-16.

INITIAL DISTRIBUTION LIST

Addressee	No. of Copies
Office of Naval Research (ONR 321: T. G. Goldsberry, K. Dial, S. Littlefield)	3
Defense Technical Information Center	12
MedAcoustics Corp. (A. Eberhardt (3), C. Chassaing (3))	6
Eastern Connecticut Cardiology Group PC (M. Fiengo (2))	2